



# Equilibrium of fluid fluxes in the wake of a three-dimensional flat-back bluff body

T.I. Khan<sup>1</sup>, L. Pastur<sup>2</sup>, O. Cadot<sup>3</sup> and V. Parezanović<sup>1,†</sup>

<sup>1</sup>Khalifa University of Science and Technology, P.O. Box 127788, Abu Dhabi, UAE

<sup>2</sup>Institute of Mechanical Sciences and Industrial Applications, ENSTA-Paris, Institut Polytechnique de Paris, 828 Bd des Maréchaux, F-91120 Palaiseau, France

<sup>3</sup>School of Engineering, University of Liverpool, Liverpool L69 3GH, UK

(Received 30 March 2024; revised 8 July 2024; accepted 26 July 2024)

The turbulent wake behind a flat-back Ahmed body is investigated using stacked stereoscopic particle image velocimetry. The wake is disturbed by a steady jet from the centre of the base and the effects are quantified for key blowing rates. The unactuated wake exhibits bistable dynamics in the horizontal plane that are completely subdued for the optimal blowing case, yielding a base drag reduction of 9%. The three-dimensional mean wake is reconstructed and used to evaluate the wake mass fluxes whose equilibrium determines the recirculation length. The results for the unactuated wake show that up to 80% of replenishment fluid flux entering the recirculation bubble from the free-stream flow is provided through the low-pressure side of the base, where the symmetry-breaking shear layer roll-up occurs near the base. For the optimal blowing configuration, where the wake becomes symmetric, the flux of wake replenishment is severely reduced. This flow configuration results in elongated shear layers on all sides, which terminate the bubble with a roll-up of reduced intensity at a further downstream location. The dominant cause of bubble growth and the accompanying drag reduction is attributed to the momentum of the base blowing, and the new regime is referred to as the ‘favourable momentum regime’. Similar trends are observed when the model is at 5° yaw where a reduction of drag and yaw-induced asymmetry are obtained. Proper orthogonal decomposition of the wake reveals the coherent structures related to the bistable flow and the symmetric wake under optimal blowing coefficient.

**Key words:** drag reduction, separated flows, wakes

† Email address for correspondence: [vladimir.parezanovic@ku.ac.ae](mailto:vladimir.parezanovic@ku.ac.ae)

## 1. Introduction

The wakes of bluff bodies are a clearly differentiated class of aerodynamics problems found in many industrial applications as either two- or three-dimensional (3-D) flows. The main feature of such flows is the presence of a massively separated, unsteady flow region (wake) behind the body that causes the dominance of pressure drag. It is well known that the low pressure at the base of a bluff body is related to the length and shape of the recirculation region. The common academic representation of a range of typical ground transport vehicles is the Ahmed body (Ahmed, Ramm & Faltin 1984) and its variations, such as the flat-back configuration used for emulating SUVs, vans and lorries. Recently, the ever increasing focus on sustainable technologies and growing concerns on energy waste and harmful gas emissions have garnered the attention of researchers to study the wake mechanisms that contribute towards drag in order to propose energy efficient drag reduction techniques (Choi, Lee & Park 2014).

The wake of a flat-back Ahmed body is known to exhibit global modes described by two distinct vortex shedding frequencies. These are associated with the shedding interaction of the shear layers emanating from the vertical and horizontal sides of the base (Grandemange, Gohlke & Cadot 2013*b*). The wake is also characterized by a ‘pumping’ phenomenon that appears as a low frequency shrinkage and expansion of the recirculation region (Volpe, Devinant & Kourta 2015). Another salient feature is the presence of a long-time steady asymmetry referred to as the reflectional symmetry-breaking (RSB) mode (Grandemange, Cadot & Gohlke 2012). The wake manifests itself as a bistability along the larger dimension of the base, switching randomly on the order of  $10^3$  convective time units. The RSB mode has been found to be sensitive to numerous factors such as base aspect ratio (Grandemange, Gohlke & Cadot 2013*a*), ground clearance (Grandemange, Gohlke & Cadot 2014; Bonnavion & Cadot 2018), perturbations (Barros *et al.* 2017; Bao *et al.* 2022), flow orientation (Haffner *et al.* 2020; Fan, Parezanović & Cadot 2022) and free-stream turbulence (Cadot *et al.* 2020; Burton *et al.* 2021). This static asymmetry induces side forces on the body and is known to contribute as an additional source of drag (Pier 2008; Cadot, Evrard & Pastur 2015; Grandemange *et al.* 2015). The drag reduction efforts are thus focused on two aspects; first to modify the size and shape of the wake and secondly through obtaining control over the RSB mode.

Different passive methods for drag reduction have been employed in the past that range from introducing some physical disturbance in the wake (Gilliéron & Kourta 2010; Grandemange *et al.* 2014) to modifying the aft section of the base using cavity or flap arrangements (Duell & George 1993; Khalighi, Chen & Iaccarino 2012; Grandemange *et al.* 2013*c*; Lucas *et al.* 2017; Bonnavion & Cadot 2019). The latter achieves base pressure recovery as a result of a boat tail effect forming a narrower wake with an extended recirculation region. Passive methods are also known to have an effect on the RSB mode. For instance, placement of a control cylinder in the wake has shown to positively influence the RSB mode achieving a drag reduction of around 4% (Grandemange *et al.* 2014). The most prominent reduction of RSB mode using passive means was achieved using a base cavity, as demonstrated by Evrard *et al.* (2016) and later confirmed by Lucas *et al.* (2017) and Bonnavion & Cadot (2018). The resulting wake is symmetrized in both horizontal and vertical directions with significant reduction in side force fluctuations along with drag decrease. These methods, albeit effective, render physical modification to the aft section geometry and are often not practical due to ergonomic or operational constraints (Hucho & Sovran 1993). Active control strategies, such as steady or pulsed blowing at or near the base, are thus explored that resort to non-intrusive means of wake modification.

For a square-back Ahmed body, base blowing is commonly performed through a different slit arrangement around the perimeter of the base (Wassen, Eichinger & Thiele 2010; Littlewood & Passmore 2012; Barros *et al.* 2016). This arrangement tends to modify the curvature of shear layers near separation resulting in a narrower wake region, an effect analogous to boat tailing (Wong & Mair 1983). On the other hand, active control over the RSB mode is often attempted through pulse jet actuation (Li *et al.* 2016; Plumejeau *et al.* 2020) and an oscillating flaps (Brackston *et al.* 2016) arrangement around the base. These methods have been shown to reduce the wake asymmetry strength, with the wake switching occurring closer to the plane of symmetry. However, these methods sometimes achieve meager drag reductions due to the increased turbulent activity of the shear layers introduced by the actuating mechanisms. Lorite-Díez *et al.* (2020*b*) attempted steady base blowing through different perimetric slit arrangements around the base. The steady blowing was effective at changing the recirculation bubble size and reducing drag, but almost no change was observed in the magnitude of wake asymmetry up to a certain blowing coefficient. Beyond that threshold, the RSB mode would shift from the horizontal to the vertical plane resulting in an introduction of a steady vertical pressure gradient. In a geometrically similar experiment, Hsu *et al.* (2021) used steady suction through a continuous slit around the perimeter of the base. The suction actuator very easily achieved a symmetric wake in both planes, however, this was accompanied by a drag increase since the recirculation bubble shrank due to mass being extracted from the wake.

Many studies have been carried out focusing on the effect of base blowing and base bleed on 3-D axisymmetric bodies (Tanner 1975; Porteiro, Przirembel & Page 1983; Suryanarayana & Meier 1995; Viswanath 1996; Sevilla & Martínez-Bazán 2004; Oxlade *et al.* 2015; de la Cruz, Oxlade & Morrison 2017). Most recently, central base blowing through a sweeping jet actuator has been used by Veerasamy *et al.* (2022) and Khan, Tajik & Parezanović (2022*b*) on the flat-back Ahmed body. The actuator's sweeping plane was aligned with the lateral wake bistability, with an idea to introduce a low momentum oscillating jet from the centre of the base. Apart from the expected drag reduction affect of base bleed (Wood 1964; Bearman 1967), the method proved to be efficient in terms of symmetrizing the wake. Our recent study using a steady jet actuator further confirms the potential of such a base blowing mechanism in achieving RSB mode suppression (Khan *et al.* 2022*a*), as opposed to base blowing being carried out near the separating shear layers. Moreover, the amount of drag reduction achieved was significantly greater compared with peripheral blowing of Lorite-Díez *et al.* (2020*b*). These studies suggest a dependence on the location, the type and the intensity of actuation to affect different mechanisms that govern the length of the recirculation region.

In the current work we analyse the wake actuated by the steady jet in terms of the simple model of Gerrard (1966) that addresses the mechanisms governing the formation length for two-dimensional (2-D) bluff bodies. He proposed that the length of the recirculation region is linked to the equilibrium of fluxes entering and exiting the region. This equilibrium of fluxes has only recently been examined in experimental measurements by Stella, Mazellier & Kourta (2017) and Stella *et al.* (2018). Considering the mean recirculating flow aft of a ramp, a flux analysis was performed on the separating line defined by the recirculation region interface (RRI). They demonstrated that a net zero is achieved when the fluxes leaving and entering through this interface are consolidated. Here, the flux entering presents the analogy of the backflow into the recirculation region that was found to scale linearly with the reattachment length. We observe that this analysis lends naturally to the model of Gerrard (1966) and has not been performed for 3-D wakes before, thus providing motivation for the present study. By obtaining 3-D flow field measurements in the wake of

an Ahmed body, we attempt to discern between the different fluxes that govern the balance of the recirculating region. At the same time, the actuation of the wake using base blowing will be used to assess how the fluxes adapt to provide drag reduction.

Apart from the mean wake balance, comprehending the dominant structures in the wake also requires a 3-D description of the flow field. Some prominent structures associated with symmetry-breaking states have been proposed by different experimental and numerical studies. Based on 2-D particle image velocimetry (PIV) measurements, Evrard *et al.* (2016) describes a horseshoe structure for the asymmetric wake that transforms to a toroid corresponding to a symmetric wake in the effect of base cavity. Using similar measurements, Perry, Pavia & Passmore (2016) proposed the existence of two structures; a large horseshoe vortex stemming from the recirculation closer to the base whereas another small horseshoe vortex that is shed faster and located farther away from the base. On the other hand, Pavia, Passmore & Sardu (2018) performed stereo PIV measurements at two downstream locations parallel to the base and, combined with the results of Perry *et al.* (2016), suggested the presence of a hairpin vortex that bends sharply to end on the opposite side of the vertical plane of symmetry. Their tomographic PIV measurements also suggest the existence of a hairpin vortex formed as an interaction of two horseshoe vortices (Pavia *et al.* 2020). The structures proposed through numerical studies somewhat contradict the notion of the presence of a single or multiple structures for bistable flows reported in experiments. Simulating bistability in the wake comes with its own challenges of the long-time scales associated with wake state switching (Evstafyeva, Morgans & Dalla-Longa 2017; Lucas *et al.* 2017; Dalla-Longa, Evstafyeva & Morgans 2019; Hesse & Morgans 2021; Ahmed & Morgans 2022; Khan, Parezanović & Afgan 2023). Most of the latter studies report the presence of a deformed or tilted low-pressure torus that becomes parallel to the base for the transient symmetric state as well as a time-averaged solution provided bistability was observed. Only in the study of Dalla-Longa *et al.* (2019) was it observed that the asymmetric wake appears to shed large hairpin structures from the farther edge of the tilted toroid. Apart from the attempt of Pavia *et al.* (2020), experimental 3-D reconstruction of the wake has been seldom attempted. In the present study we attempt to identify through proper orthogonal decomposition (POD) of the reconstructed field, the structures associated with the natural symmetry-breaking states and those resulting from base blowing.

This paper is organized as follows. In § 2 we detail the experimental set-up and measurement techniques used. Mean flow fields and the impact of blowing on wake dynamics are presented in § 3. The relevant models, methodology and analysis of wake fluxes are introduced and discussed in § 4. Major 3-D wake modes and structures are extracted using POD and presented in § 5. In § 6 we apply these approaches to the wake with side slip and blowing. The work is summarized and future avenues are proposed in § 7.

## 2. Experimental set-up

### 2.1. Wind tunnel, test model and flow actuation

The experiments were conducted in a Eiffel-type wind tunnel with test section dimensions of  $390 \times 400 \times 1200$  mm ( $h \times w \times l$ ). The wind tunnel facility, the bluff body and the pressure and force measurements were performed with the same methodology as presented in Khan *et al.* (2022a). The test model used for this experiment was the flat-back version of the original Ahmed Body (Ahmed *et al.* 1984), shown in figure 1. The model has dimensions defined by  $H = 72$  mm,  $W = 97.25$  mm, and  $L = 261$  mm. The experiments

## Equilibrium of fluxes in the wake of a 3-D bluff body

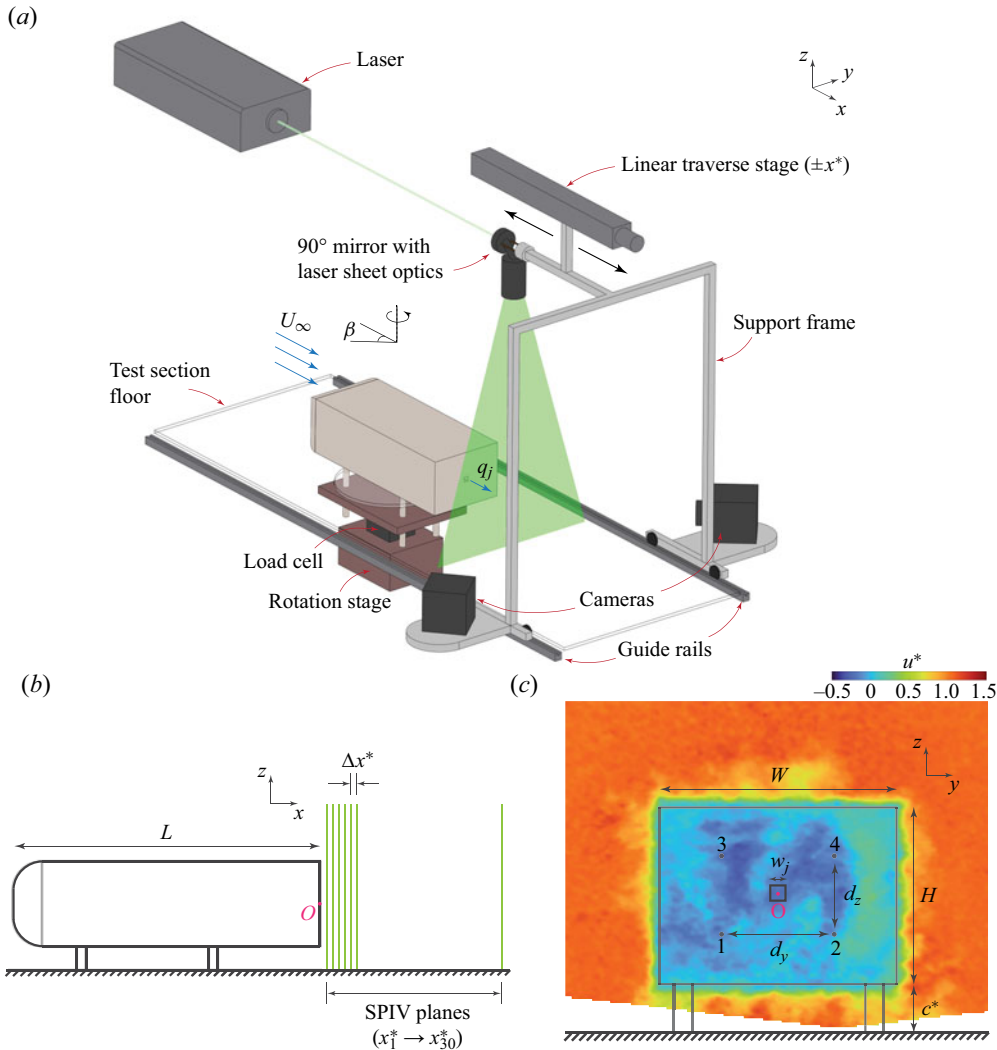


Figure 1. (a) Experimental set-up for conducting stacked stereoscopic particle image velocimetry (SSPIV). Laser is mounted at a fixed location whereas the laser sheet optics and cameras traverse in tandem. (b) Schematic of a few traversing SPIV laser planes that constitute a swept volume for constructing 3-D velocity field. First and last SPIV data acquired at  $x_1^* = 0.0694$  and  $x_{30}^* = 2.083$ , respectively, with  $\Delta x^* = 0.0694$  between the planes. (c) Rear view of the model depicting the steady jet cross-section. The SPIV field of view shown as an instantaneous streamwise velocity distribution at plane  $x^* = 0.1388$ . Location of pressure ports marked as 1, 2, 3 and 4 whereas the origin of the coordinate system is located at the centre of the base marked as  $O$ .

were performed at a free-stream velocity of  $U_\infty = 13.5 \text{ m s}^{-1}$  with a measured turbulence intensity less than 0.5%. The Reynolds number for the experiment based on the height of the body was  $Re = U_\infty H / \nu \approx 6.5 \times 10^4$ , where  $\nu$  is the kinematic viscosity. The Cartesian coordinate origin  $O(x, y, z)$  is defined at the centre of the bluff body base, where  $u, v, w$  represent the streamwise, spanwise and vertical velocity components, respectively. In the text that follows, all physical quantities have been normalized based on characteristic length, velocity and time scales ( $H, U_\infty$  and  $H/U_\infty$  respectively) and denoted with  $*$ .

The model is mounted above the test section floor keeping a ground clearance of  $c^* = 0.278$ . Four cylindrical support struts of diameter  $d^* = 0.104$  are used to mount the model on a platform that is then attached to the load balance. These hollow struts also provide access for the air supply tube to the actuator as well as tubes connecting the pressure taps to the pressure scanner. The load balance is mounted on a vertical translation and rotation stage, which helps in aligning the model to the incoming flow as well as provide yaw angle  $\beta$  to study the effects of side slip.

Flow actuation at the base of the bluff body is performed using a steady jet actuator, which is comprised of a small plenum chamber and a square duct machined from an acrylic plate. The jet is expelled through a simple square cross-section duct of side ( $w_j$ ), with a bleed-to-base area ratio of  $S_j/S = w_j^2/HW = 0.0057$ . An external 6 bar pressure source provides the air supply for actuator blowing. The mass flow rate through the actuator is controlled using an ALICAT 2000 SLPM flow controller that provides an accuracy of  $\pm 0.002 \text{ g s}^{-1}$ . The flow rate for this experiment is varied from  $0\text{--}2 \text{ g s}^{-1}$  with an increment of  $0.1 \text{ g s}^{-1}$ . The non-dimensional flow rate blowing coefficient and the momentum coefficient, is defined as

$$C_q = \frac{q_j}{U_\infty HW} \quad (2.1)$$

and

$$C_u = \frac{q_j}{U_\infty S_j} = \frac{u_j}{U_\infty}, \quad (2.2)$$

respectively, where  $q_j$  is the equivalent volumetric flow rate supplied to the actuator.

## 2.2. Velocity field measurements

Three-component velocity fields in the cross-stream planes ( $yz$ ) of the near wake of the bluff body are captured using a stereoscopic particle image velocimetry (SPIV) system. The system comprises a Litron dual-pulse laser (Nd:YAG,  $2 \times 135 \text{ mJ}$ ) synchronized with two FlowSense EO 4 Mpx cameras with a resolution of  $2048 \times 2048$  pixels each. The cameras are fitted with Nikkor 50 mm lenses and are mounted on Scheimpflug adapters. Flow seeding with atomized olive oil particles is performed at the wind tunnel inlet. Data acquisition is carried out at a rate of  $10 \text{ Hz}$  with pulse separation  $dt = 25 \mu\text{s}$ . The laser beam is deflected through a  $90^\circ$  mirror attached to laser sheet optics that provide a laser sheet parallel to the bluff body base (see figure 1*a*). The laser sheet thickness of  $4 \text{ mm}$  ( $\delta_{sheet}^* = 0.0556$ ) ensures detection of the entire range of out-of-plane (streamwise, in our case) velocities, where the minimum particle passage time through the sheet will be around  $300 \mu\text{s}$  at  $U_\infty$  used in the experiment.

The instantaneous 2-D three-component data from SPIV acquisitions in  $n = 30$  cross-stream planes (labelled as  $x_n^*$ ) are used to construct a statistically converged, 3-D velocity field, referred to as the stacked stereoscopic PIV (SSPIV) technique. To simplify velocity field acquisitions in so many parallel planes, the laser sheet optics and cameras are mounted on a common supporting frame that is displaced along guide rails in the  $x$  direction, as shown in figure 1*a*). Figure 1*b*) shows the schematic of the stacked laser sheet arrangement, where the spacing between the laser sheets is kept at  $\Delta x^* = 0.0694$ , the initial PIV plane is located at  $x_1^* = 0.0694$ , and the final acquisition is made at a downstream location of  $x_{30}^* = 2.083$ . The displacement system is aligned and calibrated such that between the planes  $x_1^*$  and  $x_{30}^*$  the dispersion of the laser beam location, where it hits the  $90^\circ$  mirror, is better than  $\pm 1 \text{ mm}$  (over a total length of  $150 \text{ mm}$ ).

The parallelism of the laser sheet (with the body base) and the focus of the cameras are confirmed by placing the Dantec SPIV target at the first and at the last plane of interest, traversing the system, and performing automatic calibrations at both ends without any further mechanical adjustment of the components. Thus, it is ensured that the quality of the imaging remains constant regardless of the streamwise location of interest and there is no need to perform recalibration of the SPIV imaging system between data acquisitions in different cross-stream planes.

In the case of the natural flow (unactuated), a total of 2000 image pairs were acquired per camera for each plane, with mean velocity convergence achieved after 1000 image pairs. For experiments with actuation that exhibit weak or no observable wake bistability, a total of 1200 image pairs were acquired per camera. The raw images were processed using TSI Insight 4G software, with three pass image cross-correlation and 50% overlap. The interrogation window for the final pass was  $16 \times 16$  pixels, which yielded  $282 \times 203$  velocity vectors in the region of interest with in-plane vector resolution of  $\delta_y^*, \delta_z^* = 0.0111$ . An example of a compound instantaneous flow field from the two cameras is shown in figure 1(c). The time-averaged vector fields obtained for all planes were interpolated to construct a 3-D velocity field within the traversed volume. The triangulation-based linear interpolation between the planes results in a vector resolution of  $\delta_x^* = 0.0111$  in the streamwise direction.

### 2.3. Pressure and force measurements

The instantaneous pressure measurements  $p_i(t)$  are obtained through four ports machined at the base of a bluff body, where  $i \in 1, 2, 3, 4$  corresponds to port locations as shown in figure 1(c), whereas the head pressure is obtained through a port at the front face of the body (not shown). Thin vinyl tubes, routed through one of the model support struts, connect these ports to a Scanivalve ZOC 22B/32Px differential pressure scanner positioned below the test section floor. All sensors, being differential, are connected to a common reference  $p_{ref}$  obtained from inside the model. Measurements are acquired at a rate of 200 Hz for a time period of  $T = 30$  s. The pressure measurement set-up is used to evaluate the effect of flow actuation on base pressure and is identical to that used in our earlier study (Khan *et al.* 2022a). The instantaneous pressure is presented as a non-dimensional pressure coefficient  $c_{p(i)} = (p_i(t) - p_{ref})/q_\infty$ , where  $p_{ref}$  and  $q_\infty = \frac{1}{2}\rho U_\infty^2$  are the mean reference static and dynamic pressures of the test section. The base pressure is expressed by a mean base suction coefficient  $C_B$ , averaged over the four pressure ports calculated as

$$C_B = -\frac{1}{4} \sum_{i=1}^4 C_{p(i)}, \quad (2.3)$$

where  $C_{p(i)} = \langle c_{p(i)} \rangle_T$  is the time-averaged value. Drag of a bluff body primarily stems from the low pressure acting at the base, hence observing variations in base pressure provide a good estimation for an overall drag variation. The effect of base blowing on bluff body drag variations can be estimated by changes in base suction defined as  $\Delta C_B = C_B - C_{B_0}$ , where  $C_B$  represents the base pressure with actuator blowing ( $U_\infty^* = 1, C_q > 0$ ) and  $C_{B_0}$  is the base pressure for the unactuated flow case ( $U_\infty^* = 1, C_q^0$ ). Apart from drag, such an arrangement of pressure ports is also sufficient to assess the changes in wake asymmetry due to flow actuation, as was demonstrated by Grandemange *et al.* (2013a). The bistability and asymmetry in wake orientation can be estimated by calculating

the instantaneous base pressure gradients in the horizontal and vertical direction as

$$g_y = \frac{c_{p(4)} - c_{p(3)} + c_{p(2)} - c_{p(1)}}{2d_y/H} \quad (2.4)$$

and

$$g_z = \frac{c_{p(3)} - c_{p(1)} + c_{p(4)} - c_{p(2)}}{2d_z/H}, \quad (2.5)$$

respectively, where  $d_y = 46$  mm and  $d_z = 32$  mm are the horizontal and vertical spacings between the pressure ports.

The horizontal base pressure gradient information is also used to perform conditional statistics on the instantaneous velocity fields. For this purpose, another set of pressure measurements is obtained during SPIV acquisition, where the pressure ports are connected to five individual high precision differential pressure sensors. The base pressure is acquired using First Sensor HCLA02X5EB whereas the head pressure is acquired using HCLA0075EB. The former has a range of 2.5 mbar, sufficient for measuring the small changes in low pressures at the base compared with a 75 mbar range sensor used for measuring the head pressure. These measurements are acquired at a rate of 1 kHz for the time period of SPIV acquisition. The PIV laser trigger signal is also acquired synchronously with the time resolved pressure signal using a National Instruments digital acquisition board. The real time information on the wake orientation (based on  $g_y$ ) along with trigger signal allows us to filter the frames according to the instantaneous asymmetry in the wake. This treatment is carried out for each downstream SPIV plane to obtain conditionally averaged vector fields.

Force measurements are obtained simultaneously using a multi-axis load balance AMTI MC3A-100 at an acquisition rate of 1 kHz. In order to estimate the effect of base blowing on the forces observed by the body, it is necessary to first determine the effect of thrust and other parasitic forces produced by the actuation. Parasitic forces in directions other than thrust may be applied to the body due to the bending of the compressed air supply tube as it is entering the bluff body and connecting with the actuator plenum, but in the remaining text we will refer to all of these as thrust force measurements for simplicity. Thrust measurements are carried out with the model installed and wind tunnel switched off ( $U_\infty^* = 0, C_q > 0$ ). Thrust data  $f_{(q)k}$  ( $k \in x, y, z$ ) is acquired for each increment of increasing flow rate with load balance and flow rate tared in between. The wind tunnel is then started and, after a settling period, force measurements  $f_k$  are acquired over the entire range of actuator flow rates ( $U_\infty^* = 1, C_q > 0$ ). The effect of thrust force is then removed from the measured force for the corresponding actuator flow rate to obtain the instantaneous force coefficient as

$$c_k = \frac{f_k - f_{(q)k}}{q_\infty HW} \quad (2.6)$$

and the corresponding mean quantities are denoted as  $C_k = \langle c_k \rangle_T$ . The variation in drag force due to increasing actuator flow rates can then be estimated as  $\Delta C_x = C_x - C_{x_0}$ , where  $C_x$  is the drag force observed with actuator blowing ( $U_\infty^* = 1, C_q > 0$ ) and  $C_{x_0}$  is the drag force for the unactuated flow case ( $U_\infty^* = 1, C_q^0$ ).

Reference measurements ( $U_\infty^* = 1, C_q^0$ ) are also acquired at the beginning and end of each experiment, and are used for drift correction of pressure and force measurements. As per manufacturer specifications, the precision of instantaneous pressure and force measurements in terms of dimensionless coefficients are  $\delta(c_p) = \pm 0.04$ ,



$\delta(c_x, c_y) = \pm 0.009$  and  $\delta(c_z) = \pm 0.018$ . However, calibration measurements performed at the start of the experiments reveal better precision values than those published by the manufacturer. The pressure scanner calibration was made using a calibrator with precision manometer (Furness Control FCO650) having an accuracy of 0.1 %. For the test supply pressure of 40 Pa, which is the typical value of base pressure for this experiment, the pressure readings across all pressure tapings was found to vary in the range of  $40 \pm 0.2$  Pa. The corresponding accuracy of base suction coefficient is estimated to be  $\pm 0.002$ . The accuracy of the load balance was checked by successively loading calibrated mass weights in the drag force direction. The obtained drag force coefficient was found to be accurate to within  $\pm 0.001$ . Similar levels of accuracy are confirmed by comparing theoretical thrust values with those obtained experimentally. Moreover, the mean values of  $C_B$  and  $C_x$  are found to satisfactorily converge after about 20 s of data, and the standard deviation of their averages over longer times (up to  $T = 30$  s) are less than 0.11 % and 0.24 % of the mean values, respectively.

### 3. Natural wake and effects of base blowing

This section will first present the unactuated baseline flow around the flat-back Ahmed body, followed by a parametric study of the base blowing actuation with respect to base suction and drag. The impact of actuation on the dynamics of the wake will be analysed using time-resolved pressure data. Finally, the static asymmetry of the wake will be evaluated using 3-D velocity fields from SSPIV, and focusing on few characteristic cases of the blowing coefficient.

#### 3.1. Baseline flow and the parametric study of base blowing

The baseline unactuated flow is presented in [figure 2\(a\)](#) using the ensemble-averaged streamlines in the horizontal ( $z^* = 0$ ) and vertical ( $y^* = 0$ ) planes. The wake appears symmetric in both orientations when averaged over the entirety of observations, confirming the general symmetry of the experiment. The length of the recirculation region ( $L_r^*$ ) is classically obtained as the maximum downstream location from the body where  $u^* \leq 0$ , as found in the  $y^* = 0$  plane. The characteristic length indicates the downstream closure of the recirculation region and is known to be directly linked to the base pressure (Bearman 1967). The unactuated wake has a recirculation length of  $L_r^* = 1.49$  that is comparable to similar studies (Grandemange *et al.* 2013*b*; Barros *et al.* 2016; Haffner *et al.* 2020). The pressure measurements at the base reveal a reference base suction coefficient  $C_{B_0} = 0.185$ , consistent with values reported in literature for similar base dimensions (Grandemange *et al.* 2014; Lorite-Díez *et al.* 2020*b*; Lorite-Díez *et al.* 2020*a*), whereas the reference drag coefficient for the present experiment is obtained as  $C_{x_0} = 0.375$ .

On shorter time scales the wake exhibits a bistable symmetry breaking clearly manifested in the time series of the horizontal base pressure gradient ( $g_y$ ), as shown in [figure 2\(b\)](#). The  $y$  instability causes the wake to switch between two equiprobable states ( $P$  and  $N$  states) about the vertical plane of symmetry (Grandemange *et al.* 2012, 2013*b*). The vertical base pressure gradient ( $g_z$ ) is not affected by this instability and remains constant at all times around zero, demonstrating a near symmetry of the flow in the vertical plane. [Figure 2\(c\)](#) shows the conditionally averaged streamlines corresponding to the  $N$  state of the wake. The characteristic asymmetry is clearly visible in the horizontal plane ( $z^* = 0$ ) by the skewed location of the vortex pair, whereas the vertical plane shows a symmetric vortex pair. The  $P$  state, being equiprobable, constitutes a mirror image of the  $N$  state in the horizontal plane (not shown here for brevity).

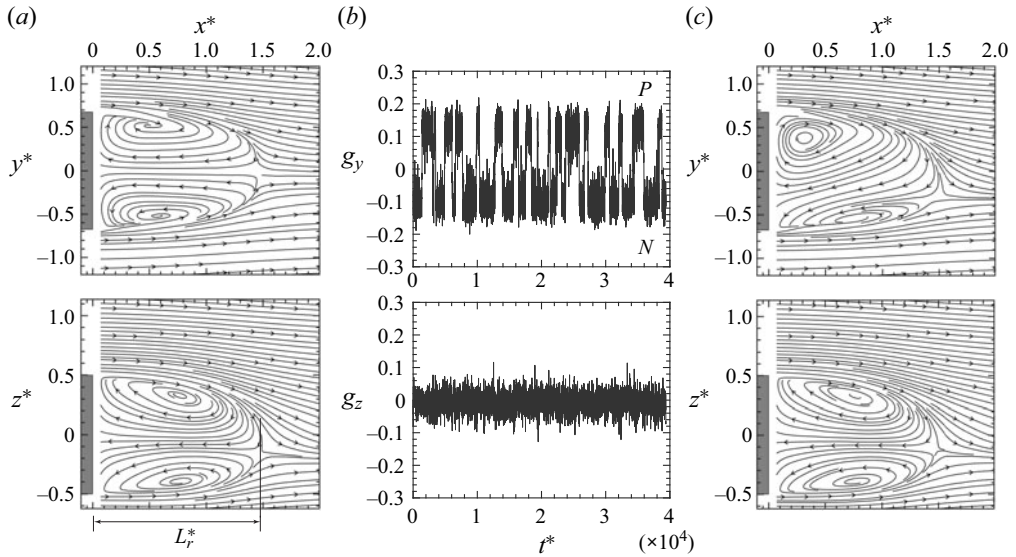


Figure 2. (a) Ensemble-averaged streamlines for the unactuated wake on the  $z^* = 0$  and  $y^* = 0$  planes. The length of the recirculation region is marked as  $L_r^*$ . (b) Time history of the horizontal ( $g_y$ ) and vertical ( $g_z$ ) base pressure gradients for the unactuated wake. The  $P$  and  $N$  states of the wake are defined by  $g_y > 0$  and  $g_y < 0$ , respectively. (c) Conditionally averaged streamlines corresponding to the unactuated  $N$  state of the wake on the  $z^* = 0$  and  $y^* = 0$  planes.

The parametric study of the effect of centralized base blowing on base suction ( $C_B$ ) and drag ( $C_x$ ) coefficients is shown in figure 3(a). Both variables are decreasing steadily as the actuation is applied up to an optimal blowing coefficient value of  $C_q^{opt} = 0.0054$ . At this intensity of actuation, the maximum reductions of  $C_B$  and  $C_x$  of around 9% and 5% are achieved, respectively. The increase of the actuation intensity beyond the optimal gradually reduces the gains and, for  $C_q > 0.013$ , results in  $C_B, C_x > C_{B_0}, C_{x_0}$ . It should be noted here that the results for  $C_x$  in the current experiment are better correlated with the variation of  $C_B$  compared with those presented in Khan *et al.* (2022a). Both studies use an identical set-up for pressure measurements and treatment of force data, but the present force measurements have been acquired using a more sensitive load balance (see § 2.3). Also, a change in the initial linear behaviour of  $C_B$  and  $C_x$  can be observed from around  $C_q > 0.02$ , where the progression becomes nonlinear leading to a minimum. This was especially not so clearly observed with the less sensitive force balance in the previous work. We will return to this change in § 4.

The efficiency of steady jet actuation is evaluated in terms of the power required for flow injection ( $\dot{m}_j u_j^2$ ) compared with the power required to overcome the aerodynamic drag ( $q_\infty S \Delta C_x U_\infty$ ). At  $C_q^{opt}$ , it is found that the actuation accounts for  $\approx 46\%$  of the maximum aerodynamic power saving. It is reiterated that the drag reduction has been evaluated after removing the effect of thrust and is purely a consequence of the wake reorganization under the effect of actuation. Adding the effect of thrust reduces the actuation power requirement to 30% of the overall aerodynamic power saving.

Figure 3(b) shows the relationship between changes in base suction ( $\Delta C_B$ ) and drag ( $\Delta C_x$ ) for different flow rates. The base blowing has no authority on the flow upstream of the trailing edge separation; once the thrust has been removed from the resultant force in the streamwise direction it follows that the changes in drag must be solely due to the

## Equilibrium of fluxes in the wake of a 3-D bluff body

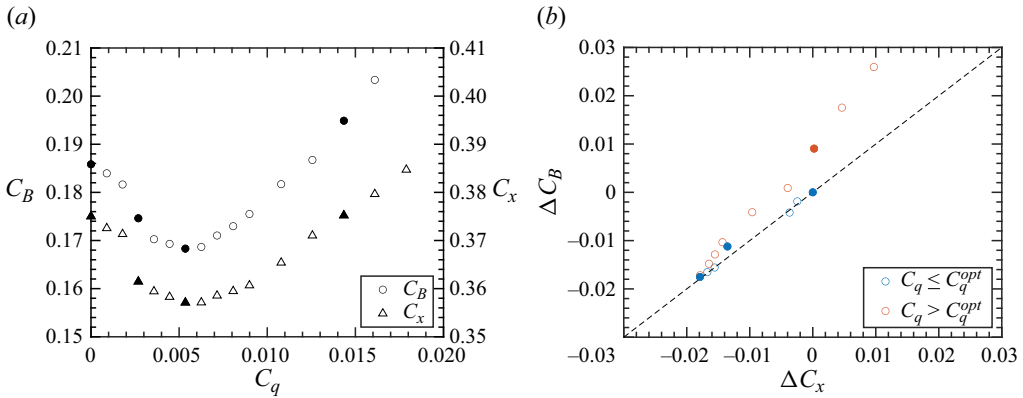


Figure 3. (a) Effect of base blowing on base suction coefficient ( $C_B$ ) and drag coefficient ( $C_x$ ). (b) Relationship between relative differences of base suction coefficient ( $\Delta C_B$ ) and drag coefficient ( $\Delta C_x$ ). Dashed line depicts the linear relation  $\Delta C_B = \Delta C_x$ . The filled markers correspond to flow rates at which SSPIV measurements have been conducted (see § 3.3).

modification of the base pressure. Thus, the relative reduction of base suction is expected to translate directly into a relative drag reduction (absolute values are linearly dependent). As observed in figure 3(b),  $\Delta C_B = \Delta C_x$  is obtained fairly consistently for  $C_q \leq C_q^{opt}$  but diverges for  $C_q > C_q^{opt}$ , where the average of the four pressure port measurements is no longer an accurate representation of the base suction due to the presence of a strong jet. The only point that deviates noticeably from the slope of 1 is for  $C_q = 0.0027$ , where the change from linear to nonlinear behaviour versus  $C_q$  occurs. Here, we can notice that the  $C_B$  value in figure 3(a) is shifted towards the middle between its adjacent neighbours, whereas the equivalent value of  $C_x$  is much closer to the subsequent value at the next higher  $C_q$ .

In order to understand the interactions of base blowing with the flow, SSPIV measurements are performed for four characteristic actuator flow rate regimes highlighted by filled markers as shown in figure 3. The corresponding blowing coefficients are the unactuated flow with  $C_q^0 = 0$ , low intensity blowing  $C_q^{lo} = 0.0027$ , optimal (minimum drag) blowing  $C_q^{opt} = 0.0054$  and high intensity blowing  $C_q^{hi} = 0.0143$ . In the following sections we will focus on these four cases when analysing and discussing the available data.

### 3.2. Base blowing and wake dynamics

In the following we analyse the wake dynamics using the time-resolved base pressure data obtained synchronously with the PIV measurements. A segment of the  $g_y(t^*)$  and  $g_z(t^*)$  base pressure gradient time signals are shown in figure 4(a) for the four characteristic blowing rates. As established previously, the time series of  $g_y(t^*)$  for  $C_q^0$  reveal a clear bistable behaviour in the horizontal pressure gradient. This behaviour is strongly modified for the  $C_q^{lo}$  case, where the switches between the  $P$  and  $N$  states are much more frequent and the maximum  $g_y$  is slightly reduced. The  $g_y(t^*)$  series in the case of  $C_q^{opt}$  and  $C_q^{hi}$  show a complete damping of the static asymmetry exchanges and the presence of only small amplitude fluctuations of the horizontal pressure gradient around zero. For  $C_q^0$ ,  $C_q^{lo}$  and  $C_q^{opt}$ , the vertical pressure gradient  $g_z$  exhibits small amplitude, high frequency fluctuations

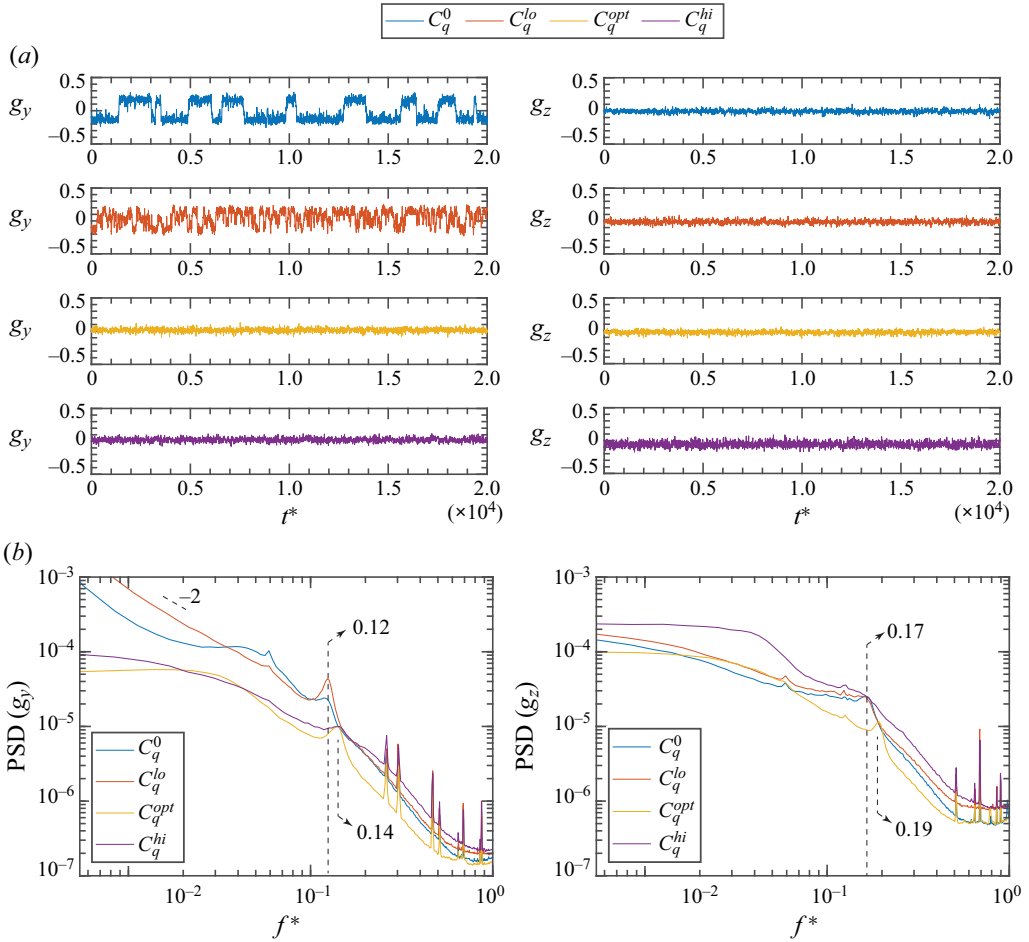


Figure 4. Effect of base blowing on the dynamics of base pressure gradients  $g_y$  and  $g_z$ : (a) time series and (b) power spectral densities (PSDs), for four base blowing coefficients.

around a zero value. For the case of  $C_q^{hi}$ , the  $g_z$  no longer oscillates strictly around zero but around a finite negative value, indicating that the vertical symmetry of the wake has been altered. In addition, we can observe an increased amplitude of high frequency fluctuations of  $g_z(t^*)$ . We can conclude that the wake asymmetry is highly sensitive to central base blowing, which is a significant departure from the behaviour observed for trailing edge base blowing in Lorite-Díez *et al.* (2020b).

Figure 4(b) shows the spectral analysis of the above signals that are useful to assess both the static and the periodic modes of the wake dynamics. The power spectral densities (PSDs) reveal the characteristic frequencies associated with the wake of such bodies. As mentioned, the time series used in figure 4(a,b) are obtained during SPIV acquisitions, where pressure measurements for all 30 PIV planes were combined to produce a large data set (over  $t^* = 1 \times 10^6$ ) and a well-resolved spectrum for each of the four configurations. The spectral density estimation is carried out using Welch's method with 50% overlap. A Hamming window is used and the resulting spectra has a resolution of  $\Delta f^* = 0.0025$ , where  $f^* = fH/U_\infty$ . The characteristic frequencies in the unactuated wake ( $C_q^0$ ) are observed as energy peaks at  $f^* = 0.12$  in  $\text{PSD}(g_y)$  and 0.17 in  $\text{PSD}(g_z)$ . These frequencies

## Equilibrium of fluxes in the wake of a 3-D bluff body

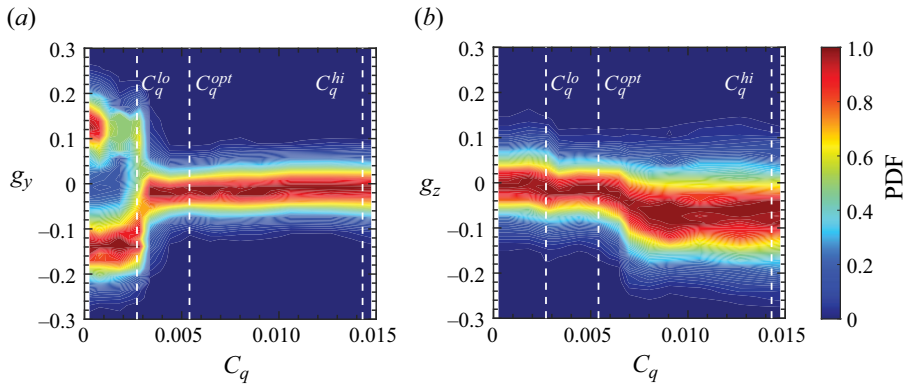


Figure 5. Effect of base blowing on static mode. Sensitivity map of the horizontal ( $g_y$ ) and vertical ( $g_z$ ) base pressure gradient. White dashed lines corresponds to increasing flow rates  $C_q^{\text{lo}}$ ,  $C_q^{\text{opt}}$  and  $C_q^{\text{hi}}$ .

are reminiscent of the two periodic modes of shedding related to interactions between the opposing free shear layers in the horizontal and vertical orientations, respectively (Grandemange *et al.* 2013*b*). A broadband energy accumulation is also observed around  $f^* \approx 0.06$  in  $\text{PSD}(g_y)$  that is attributed to the bubble pumping dynamics as described by Volpe *et al.* (2015). For  $C_q^{\text{lo}}$ , an increased peak amplitude at  $f^* = 0.12$  in  $\text{PSD}(g_y)$  suggests a strengthening of lateral shedding dynamics, whereas no change in vertical shedding dynamics in  $\text{PSD}(g_z)$  is observed. The bistable dynamics of the wake, characterized by a power law slope of  $-2$  in the very low frequency band (say  $10^{-3} < f^* < 10^1$ ) in the  $g_y$  signal, are clearly observable for the  $C_q^0$  and  $C_q^{\text{lo}}$  cases, albeit with a different distribution of energy. As observed earlier from the time series, the blowing at  $C_q^{\text{lo}}$  causes a more continuous redistribution of fluctuating energy across the very low frequency band and up to the band of the Volpe frequency that is no longer visible. For  $C_q^{\text{opt}}$ , a clear reduction in bistable dynamics is observed with diminishing slope and energy levels for  $f^* < 10^{-1}$ . Interestingly, the Strouhal number of the vortex shedding is now shifted for both  $g_y$  and  $g_z$  to new values of  $f^* = 0.14$  and  $f^* = 0.19$ , respectively, and associated with a strong reduction of fluctuation energy, indicating a damping of the two periodic global modes. Finally, for  $C_q^{\text{hi}}$ , a broadband peak of low amplitude is present around  $f^* = 0.14$  in  $\text{PSD}(g_y)$  but no discernible peak is found in  $\text{PSD}(g_z)$ . For this regime, the fluctuation energy globally increases for the entire measurable range of  $f^*$ , which is likely the signature of the strong blowing jet.

### 3.3. Static mode of the wake under actuation

The bistable wake dynamics comprise random switches between two opposite states of a static symmetry-breaking mode. Figure 5 shows the sensitivity of the symmetry-breaking mode to base blowing, based on the normalized probability density function (PDF) of the base pressure gradient components. The wake is initially defined by the two equiprobable peaks in the  $g_y$  map corresponding to  $P$  and  $N$  states. With increasing  $C_q$ , the bi-modal PDF evolves towards a mono-modal pattern around  $C_q \approx 0.003$ , suggesting a suppression of the static mode that prevails thereafter. The minimum strength of the static mode is achieved at  $C_q^{\text{opt}}$ , as observed by the minimum thickness of the distribution. On the other hand, the sensitivity map of  $g_z$  appears symmetric in the vertical orientation and remains

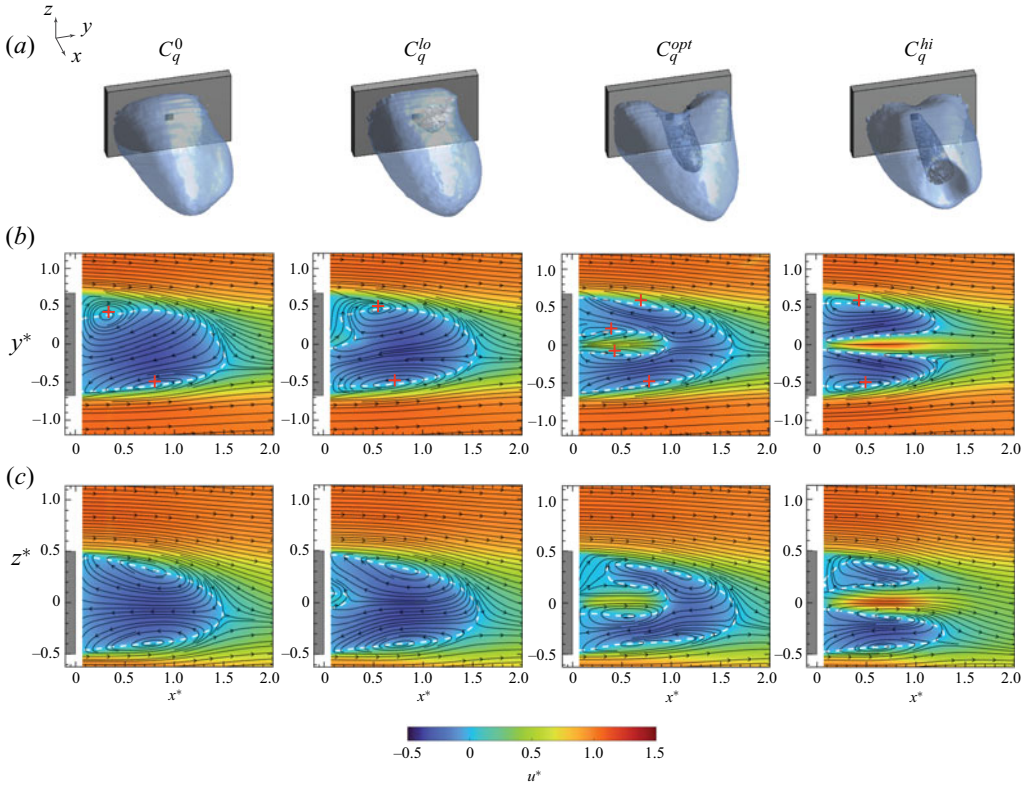


Figure 6. Global changes to the mean (conditionally averaged) 3-D recirculation bubble visualized through the isosurface of  $u^* = 0$  for  $C_q^{PIV}$  cases. The darker shade surface indicates the jet confined within the main recirculation bubble. Corresponding mean streamwise velocity distribution overlaid with streamlines are shown at  $z^* = 0$  and  $y^* = 0$  planes. The white dashed line represents the recirculation bubble as an isoline of  $u^* = 0$ . Markers (+) indicate the recirculating vortex core locations observed on  $z^* = 0$  plane.

unaffected till the optimal flow rate. After  $C_q \approx 0.007$ , the PDF adopts a slightly negative orientation with a wider spread influenced by the high momentum jet.

The global effect of base blowing on the 3-D recirculation bubble is visualized through the changes to the isosurface of  $u^* = 0$  from conditionally averaged flows, as shown in figure 6. The conditionally averaged data are obtained by sampling the SSPIV frames based on the horizontal base pressure gradient  $g_y < 0$  to extract the  $N$ -state wake. For the  $C_q^{opt}$  and  $C_q^{hi}$  cases, the obtained conditionally averaged wake was observed to be identical to the ensemble average (on the entirety of samples). Hence, for these cases ( $C_q^{opt}$  and  $C_q^{hi}$ ), an ensemble average is presented in figure 6 to obtain better statistical convergence of the velocity field. The corresponding streamline distribution of the recirculating flow is shown in figure 6 on the extracted horizontal  $z^* = 0$  and vertical  $y^* = 0$  planes.

The  $N$ -state wake for  $C_q^0$  is described by the stronger recirculating vortex close to the base behind the right side of the body, whereas the opposite vortex is stretched and its core located further downstream (see red + markers in  $z^* = 0$  plane velocity field in figure 6). The dashed lines represent the boundary shape of the recirculation bubble in the plane of interest. For  $C_q^{lo}$ , the low momentum jet is biased to the right side ( $y^* > 0$ ) of the base due to its interaction with the larger circular vortex that also effects the bubble closure near

the base. This results in a realignment of the recirculation vortex cores reducing the wake asymmetry, as evidenced by the respective  $x^*$  coordinates of the vortex cores in the  $z^* = 0$  plane. The situation is similar and opposite for the  $P$  state, which is omitted here. A slight increase in bubble length to  $L_r^* = 1.55$  is observed for  $C_q^{lo}$ .

The mean recirculating vortex core realignment is further enhanced for the  $C_q^{opt}$  case, such that the streamlines present an almost perfectly symmetric wake with the steady jet prominently visible within the main recirculation bubble. Another pair of symmetric recirculation vortices, belonging to the steady jet flow, is found closer to the base and to the streamwise axis of symmetry. The recirculation length is significantly increased to  $L_r^* = 1.66$  and associated with the minimum drag. It can, however, be observed in the  $y^* = 0$  plane that the jet for  $C_q^{opt}$  interacts with the upper side of the recirculation bubble near the body base, somewhat similar to what was observed in the  $z^* = 0$  plane for the  $C_q^{lo}$  configuration. The bias to the upper side is likely due to the general vertical asymmetry imposed by the ground effect.

For the case of the high momentum jet  $C_q^{hi}$ , the jet now visibly occupies the centre area of the wake around the streamwise axis of symmetry and creates a toroid-shaped recirculation bubble around itself. As a consequence, two separate recirculation regions are visible in each  $z^* = 0$  and  $y^* = 0$  planes, with significantly reduced recirculation lengths, the maximum being  $L_r^* = 1.28$ . This imposes a strong low-pressure region at the base of the body that results in an increased drag. The asymmetric bubbles visible on the  $y^* = 0$  plane contribute to the negative  $g_z$  gradient associated with high flow rate. The  $C_q^{hi}$  case features a very different wake topology compared with other cases and will not be considered in the subsequent detailed analysis of the wake fluxes.

#### 4. Equilibrium of mass fluxes in the mean wake

In this section we present the balance of the mean wake fluxes and how they are modified by actuation to establish a new equilibrium in each blowing configuration.

##### 4.1. Wake equilibrium model

The starting point for this analysis is the model proposed by Gerrard (1966), which describes the 2-D cylinder recirculation region length as a consequence of an equilibrium of fluid fluxes entering and exiting the region. These fluxes are driven by the large rolling-up vortices at recirculation bubble closure and by the entrainment of the separated shear layer before its roll-up. Although the model is originally discussed for the case of the transitional flow around a 2-D circular cylinder before the drag crisis ( $10^3 < Re < 5 \times 10^4$ ), its general principles of fluid entrainment and induced velocity are applicable to any incompressible Reynolds number flow, and have been used successfully to interpret the mean recirculation bubble behaviour for other 2-D cylinder shapes (Parezanović & Cadot 2012), as well as for the flat-back Ahmed body (Lorite-Díez *et al.* 2020b). In the following we consider the flow data of the reconstructed mean wake to account for these fluxes and deduce how the wake equilibrium is achieved. This approach has never before been tested for 3-D flows.

For the flat-back Ahmed body at the Reynolds number of  $6.5 \times 10^4$  in our experiment, a 3-D turbulent wake is clearly present along with a turbulent shear layer separation at the trailing edges. The recirculation bubble is closed by shear layers rolling-up into vortices that are shed at the characteristic Strouhal number (in this case two different

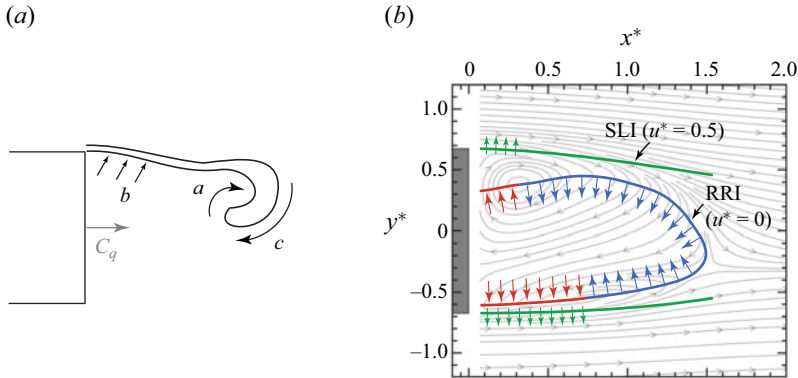


Figure 7. (a) Sketch of the separated shear layer from one of the sides of the bluff body base and different mass fluxes contributing to the recirculation length equilibrium (see text). (b) Illustration of the interfaces (RRI and SLI) through which the wake fluxes are evaluated. Coloured arrows indicate the sense of the various fluxes along the direction normal to the respective interface.

ones), creating a global mode that is much more complicated and less pronounced than in the 2-D case. Nevertheless, the separated shear layers from the four sides of the body act through their entrainment capacity and along their length to evacuate the flow out of the recirculation region, while the vortex roll-up at bubble closure first induces the flow into the recirculation region from outside but then entrains and evacuates it when it itself is shed downstream.

Figure 7(a) illustrates the different wake fluxes based on the interpretation of the model of Gerrard (1966) by Lorite-Díez *et al.* (2020b) for the case of the Ahmed body. Mass is being exchanged between the recirculation region and the surrounding environment by entering at the bubble closure through the vortex induced replenishment influx ‘c’, and exiting through the roll-up vortex engulfment outflux ‘a’, and the entrainment outflux of the turbulent shear layer ‘b’. In our experiment, there is also an optional mass flux added by the actuator at the base ( $C_q$ ). The resulting balance of fluxes ( $\Phi$ ) takes the form:

$$\underbrace{\Phi_a + \Phi_b}_{\Phi_{out}} = \underbrace{\Phi_c + \Phi_q}_{\Phi_{in}}. \tag{4.1}$$

This conceptual approach can be characterized in practice on a mean flow field as described by Stella *et al.* (2017, 2018) for the simple mass-entrainment model applied to a 2-D ramp flow. In their case, an interface through which the flow is exchanged between the wake and the free stream is defined from the mean velocity field on  $u^* = 0$ , which is called the RRI. This is illustrated in figure 7(b) with the  $u^* = 0$  isoline overlaid on the streamlines in the  $z^* = 0$  plane of the unactuated  $N$ -state flow in our experiment. Following the direction of streamlines crossing the interface, it is clear that one portion of this interface admits fluid and another portion expels fluid out of the recirculation region. The influx and outflux through the RRI is indicated by blue and red arrows, respectively. These fluxes are defined in Stella *et al.* (2018) as simply  $\Phi_{in}$  and  $\Phi_{out}$ . Here,  $\Phi_a$  and  $\Phi_b$  are indiscernible from one another and can only be assessed as a combined flux of fluid removal, i.e.  $\Phi_{a+b}$ . Flux  $\Phi_q$  is also not separately accounted for by this approach but its value is known through precisely controlled actuator mass flow rate. The latter flux should be thus assigned to the combined  $\Phi_{in}$  and can be easily discerned from the ingestion of fluid into the recirculation bubble through its closure flux  $\Phi_c$ . Application of this model to different wake configurations is discussed in § 4.2.



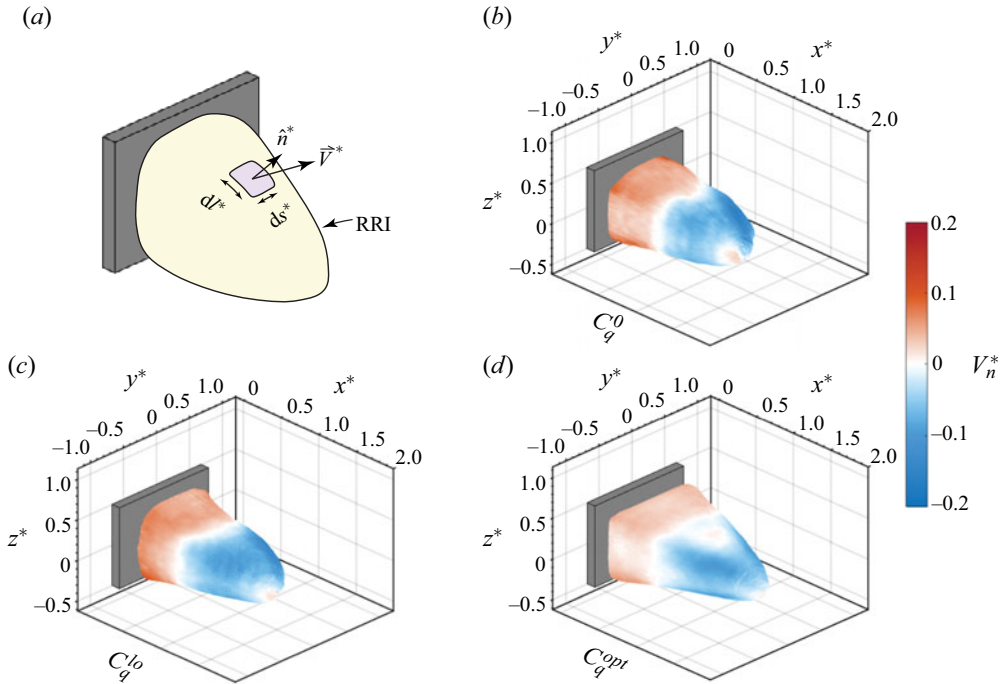


Figure 8. (a) Schematic of flux calculation ( $\Phi_{a+b}$ ,  $\Phi_c$ ) through the RRI discretized along the perimeter  $ds^*$  and length  $dl^*$ . Normal velocity ( $V_n^*$ ) distribution on the conditionally averaged  $N$ -state bubble surface for (b)  $C_q^0$ , (c)  $C_q^{lo}$  and (d)  $C_q^{opt}$  flow rates. Negative values contribute to flux  $\Phi_c$  feeding the recirculation region, whereas positive values contribute to extraction of flux  $\Phi_{a+b}$ .

In addition to the mass-entrainment model we also propose to assess the entrainment of the shear layers only, thus resolving the  $\Phi_b$  flux. A shear layer interface (SLI) is defined that corresponds to the average location of the maximum shear, using the velocity isolate at  $u^* = 0.5$  (see figure 7b). The flux through the SLI is based on entrainment velocity  $V_E^*$  for a steady shear layer, as previously used by Lorite-Díez *et al.* (2020b). This approach assumes that each separating shear layer behaves similar to a steady planar mixing layer over a certain length before being modified by the unsteady wake dynamics. The important task here is to estimate such a length and derive plausible conclusions on how the shear layer entrainment flux contributes to the recirculation bubble equilibrium. The analysis of fluxes through the SLI for our experimental configurations is discussed in detail in § 4.3.

#### 4.2. Total mass exchange through the wake boundary

We now apply the mass-entrainment model to account for the fluxes through the 3-D RRI, which is illustrated in figure 8(a). A control volume is defined by the surface of the recirculation bubble ( $u^* = 0$ ), equivalent to the RRI, which is bounded by the wall at the base through which only  $\Phi_q$  enters. The estimate of the total flux exchange across the RRI based on the normal velocity component on the surface is calculated as

$$\Phi_{a+b} = \iint V_n^{*(+)} ds^* dl^* = \Phi_c = - \iint V_n^{*(-)} ds^* dl^*, \quad (4.2)$$

where  $V_n^* = \mathbf{V}^* \cdot \mathbf{n}^*$ , and  $ds^*$  and  $dl^*$  represent the surface discretized along the cross-sectional perimeter and along the length. The normal velocity distribution splits the

Case	State	$\Phi_{a+b}$	$\Delta_{a+b}$	$\Phi_c$	$\Delta_c$
$C_q^0$	$\Sigma$	0.0703	—	0.1331	—
	$N$	0.0792	12.6 %	0.1527	14.7 %
	$P$	0.0771	9.7 %	0.1529	14.8 %
$C_q^{lo}$	$\Sigma$	0.0768	—	0.1311	—
	$N$	0.0788	2.6 %	0.1359	3.6 %
	$P$	0.0777	1.1 %	0.1375	4.8 %
$C_q^{opt}$	$\Sigma$	0.0512	—	0.0984	—
	$N$	0.0520	1.5 %	0.0991	0.7 %
	$P$	0.0522	1.9 %	0.0993	0.9 %

Table 1. Values of outflux  $\Phi_{a+b}$  and influx  $\Phi_c$  through the RRI for the ensemble-averaged wake and the asymmetric  $N$  and  $P$  states for different  $C_q$ . The percentage of relative difference between the ensemble and conditional average is presented as  $\Delta = [(\Phi(N, P) - \Phi(\Sigma))/\Phi(\Sigma)] \times 100$ .

RRI into two regions; the part closer to the base associated with outflux ( $\Phi_{a+b} \forall V_n^{*(+)}$ ), and the downstream part responsible for influx into the recirculation region ( $\Phi_c \forall V_n^{*(-)}$ ), as shown in figure 8(b–d) by red and blue colours, respectively.

It is well understood that the ensemble-averaged wake is not a representative mean flow for the cases where a strong asymmetry is present at short time scales, as for the configurations  $C_q^0$  and  $C_q^{lo}$  in our experiment. However, we choose to apply the above analysis to both ensemble-averaged ( $\Sigma$ ) and conditionally averaged ( $P$  and  $N$ ) flows for all configurations so that we can emphasize the differences between respective states in terms of flow fluxes. The flux values obtained for the  $C_q^0$ ,  $C_q^{lo}$  and  $C_q^{opt}$  cases are presented in table 1.

The influx  $\Phi_c$  represents the requirement of the fluid to replenish the cavity behind the bluff body; for the unactuated wake, a significant difference is observed between the ensemble-averaged and conditionally averaged wakes, where the latter two are found to have an increased influx of around 15 % compared with the ensemble average. For  $C_q^{lo}$ , the  $P$ - and  $N$ -state wakes require  $\approx 4$  % greater  $\Phi_c$  than the  $\Sigma$  wake, whereas for  $C_q^{opt}$ , the difference reduces down to  $\approx 1$  %. The outflux  $\Phi_{a+b}$  follows a similar trend of  $\Phi_c$ , with the outflux being greater for the asymmetric wake compared with the ensemble-averaged flow field. It is evident that the ensemble-averaged flow is not an accurate representation of a wake that dwells in two static asymmetric states. For example, the ensemble-averaged shear layers do not physically exist since they are obtained through superposition of the two mirrored anti-symmetric configurations. Hence, moving forward, we will consider the  $N$ -state wake for further analyses, as it represents the actual flux requirement of the wake and the effect of additional flux  $\Phi_q$  will be evaluated in light of (4.1).

The evolution of flux values ( $\Phi_{a+b}$ ,  $\Phi_c$ ) for the  $N$ -state wake is presented in figure 9(a) as an increasing recirculation region length ( $L_r^*$ ). A significant difference is observed between the two quantities where  $\Phi_{a+b} < \Phi_c$ , which ought to compensate each other according to the equilibrium model. This difference stems from the missing SSPIV data near the base, which fails to account for the complete outflux  $\Phi_{a+b}$ . To estimate the influence of this small region close to the base, we evaluate the integral of the total flux ( $\Phi_{out} + \Phi_{in} = \Phi_{a+b} + \Phi_c + \Phi_q$ ) entering and leaving the control volume along the streamwise direction, as shown in figure 9(b). Considering the unactuated flow case first ( $\Phi_q = 0$ ), the integral should yield a zero at the end of the recirculation region ( $x^* = L_r^*$ )

## Equilibrium of fluxes in the wake of a 3-D bluff body

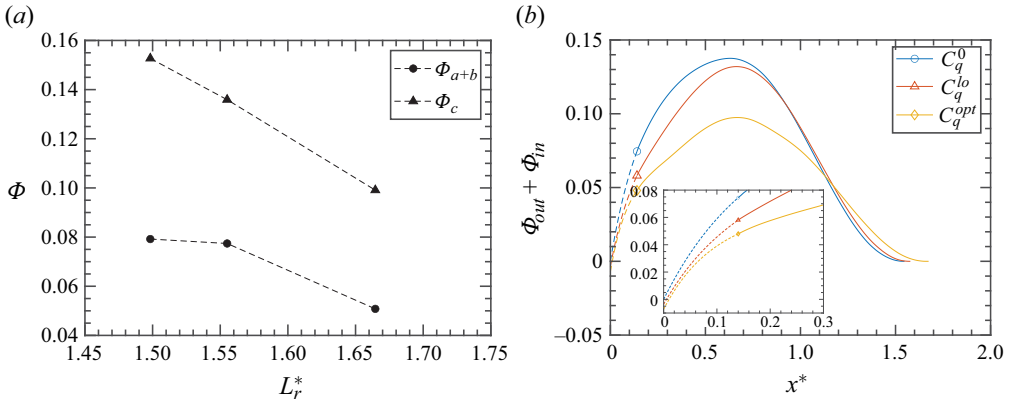


Figure 9. (a) Total flux leaving ( $\Phi_{a+b}$ ) and entering ( $\Phi_c$ ) through the RRI. (b) Integral of the total flux ( $\Phi_{a+b} + \Phi_c + \Phi_q$ ) as a function of streamwise location for respective flow rates. Dashed lines represent a polynomial extrapolation to account for the missing PIV data near the base.

due to conservation of mass. The missing data then presents a nonlinear behaviour near the base that is obtained using polynomial extrapolation (dashed curve) that again yields a zero at the start of the recirculation region. Base blowing further aggravates this issue as visible by curve extrapolation near the base for  $C_q^{lo}$  and  $C_q^{opt}$  cases in figure 9(b). For these two cases, the curve is shown to start at a negative offset value corresponding to  $\Phi_q$  at the base (refer to inset). Nevertheless, we can identify the challenges associated with this approach to accurately account for the flux leaving the recirculation region and achieve the balance of (4.1). On the other hand, the flux  $\Phi_c$  for all the cases is completely accounted for and can be used to determine the global requirement of the influx of the outside flow into the recirculation region. A convergence check on this flux estimation is carried out for the last 100 PIV snapshots, which gives a standard deviation  $\sigma(\Phi_c) = 6 \times 10^{-5}$ . Flux estimation is also carried out using a coarsened discretization of the RRI ( $ds^*/2, dl^*/2$ ). Similar values of  $\Phi_c$  are obtained for all cases with a difference of less than 0.6%, indicating that the characteristic surface is sufficiently discretized.

From the results presented above, we can observe that an increase in  $C_q$  and the concomitant elongation of the recirculation region ( $L_r^*$  increased) cause an important reduction of  $\Phi_c$ . Since this flux is associated with bubble closure, we evaluate the changes to the global mode associated with vortex shedding in terms of velocity fluctuations. The global mode is defined by the modulus of spanwise and vertical velocity fluctuations as  $\sqrt{v'^*{}^2 + w'^*{}^2}$ . Figure 10(a-c) shows the distribution of this mode on the  $y^* = 0$  and  $z^* = 0$  half-planes for different flow rates. For  $C_q^0$ , the maximum of this mode is highest of all three configurations and located in a narrow range of streamwise locations  $1.2 < x^* < 1.5$ , corresponding to the recirculation region length  $L_r^* = 1.49$ . For the case of  $C_q^{lo}$ , the global mode maximum is notably reduced and saturates over a wider range of  $1.3 < x^* < 1.8$ . Finally, the  $C_q^{opt}$  case presents a significantly diminished strength of this mode. The effect is quantified in figure 10(d), which shows the values extracted along the centreline of the base in the streamwise direction  $(x^*, 0, 0)$ . We can clearly observe that with base blowing, the magnitude of these fluctuations are reduced whereas the maxima are shifted downstream. High levels of fluctuations observed near the base for the  $C_q^{opt}$  case are introduced by the jet and the effect gets diminished around  $x^* = 1$ , beyond which the strength and location of the global mode can be discerned. These results indicate

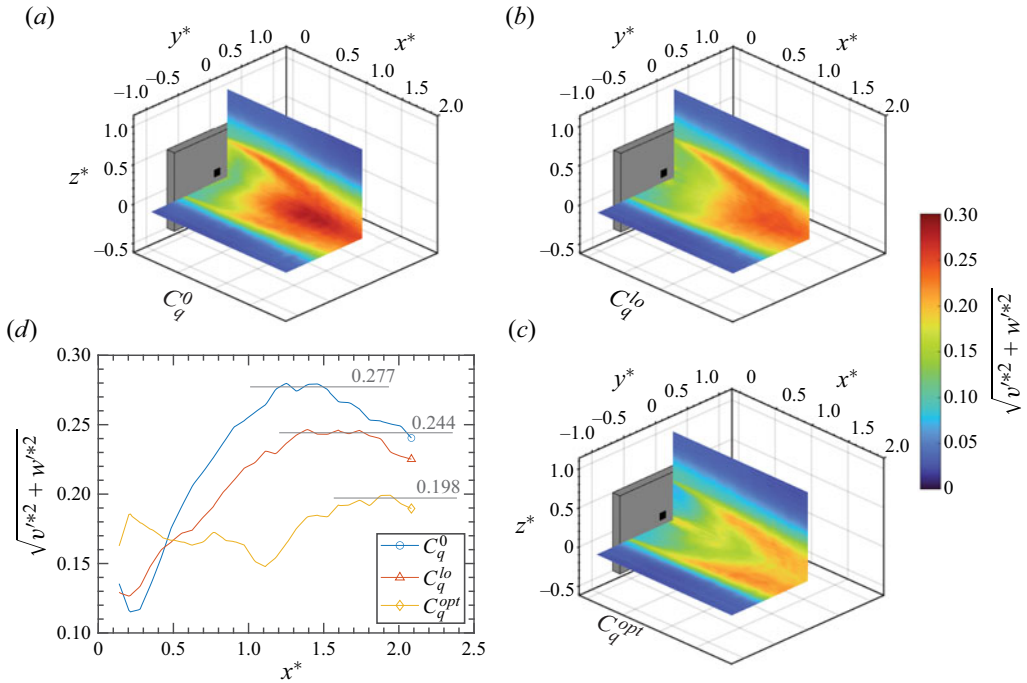


Figure 10. Distribution of the global mode strength defined as the modulus of spanwise and vertical velocity fluctuations on  $y^* = 0$  and  $z^* = 0$  half-planes for (a)  $C_q^0$ , (b)  $C_q^{lo}$  and (c)  $C_q^{opt}$  flow rates. (d) Plot showing the values extracted along the centreline of the base ( $y^*, z^* = 0$ ).

that the weakening of the shedding roll-up may contribute to the reduction of induced replenishment flux into the recirculation region.

We can conclude that an increase in the recirculation bubble length is coupled with a damping of the vortex shedding global mode, in a similar way to what has been observed for 2-D wakes (Parezanović & Cadot 2012). The global mode damping causes less fluid to be admitted per unit of time into the recirculation region ( $\Phi_c$ ), although the recirculation region itself is growing in size. At the same time, the expulsion of fluid from the recirculation region related to flux  $\Phi_{a+b}$  is also diminished. By continuity, this outflux should compensate the influx, although we could not confirm this with direct measurements. Nevertheless, extrapolation presented in figure 9(b) presents a plausible evolution of the outflux in the region of missing data for an equilibrium of the recirculation bubble, subject to the principle of mass conservation. Therefore, we can conclude that a larger recirculation region behind a bluff body equates to a lower exchange rate of fluid between the wake and the surrounding free-stream flow.

### 4.3. Shear layer entrainment flux

In this section we endeavor to isolate the entrainment flux through the shear layers  $\Phi_b$ , from the combined outflux  $\Phi_{out}$ . As introduced in § 4.1, a SLI is defined to represent the surface of separated shear layers. Figure 11(a) shows the magnitude of shear computed in a generalized form as

$$\frac{du^*}{dn^*} = \sqrt{\left(\frac{du^*}{dy^*}\right)^2 + \left(\frac{du^*}{dz^*}\right)^2}, \quad (4.3)$$

Equilibrium of fluxes in the wake of a 3-D bluff body

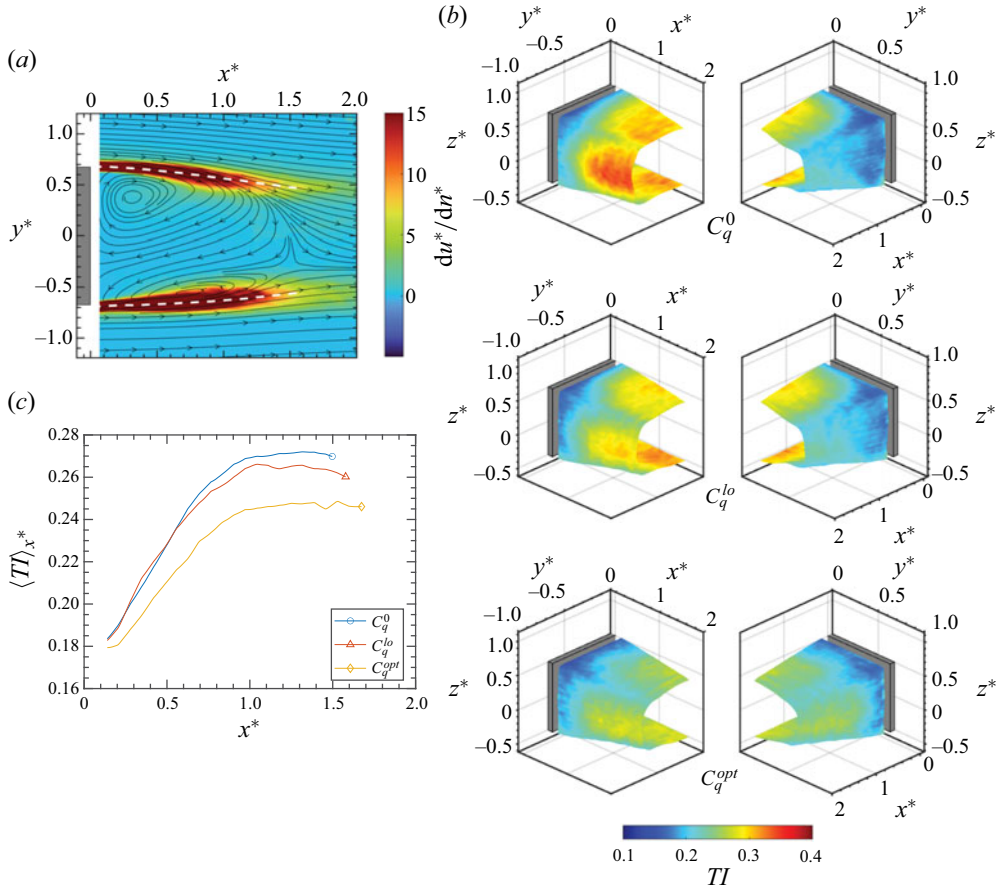


Figure 11. Shear layer surface characterization. (a) Shear distribution ( $du^*/dn^*$ ) on the  $z^* = 0$  plane, where maximum shear values correspond to locations of separated shear layers. White dashed isolines corresponds to SLI. (b) Distribution of turbulent fluctuations within the shear layers characterized on the surface of SLI. (c) Average turbulence intensity as a function of streamwise location for respective flow rates.

where  $du^*/dz^* = 0$  in the shown  $z^* = 0$  plane and the SLI (dashed line,  $u^* = 0.5$ ) is overlaid for reference. We can see that the SLI corresponds well to the regions of maximum shear that represent the average location of the separated shear layers. The resulting SLI surface for different blowing configurations is shown in figure 11(b), with the turbulent fluctuations (colour map overlay) within the shear layers evaluated in terms of turbulence intensity, classically defined as

$$TI = \sqrt{u'^{*2} + v'^{*2} + w'^{*2}}. \quad (4.4)$$

A high level of turbulence intensity is observed for the  $C_q^0$  case on the left side of the wake that, for the  $N$  state, is the side where the shear layer is preserved and grows for a longer downstream distance. On the opposite side, where the large recirculation can be seen in the mean flow streamlines (see figure 11a), the fluctuations are reduced, at least along the SLI. Blowing at  $C_q^{lo}$  results in a symmetrizing effect on the wake, which is evident by decreased levels of turbulence in the left shear layer along with a concomitant increase in the opposite right shear. A significant reduction in maximum  $TI$  is observed for

the  $C_q^{opt}$  case, which is now shifted downstream and redistributed among all shear layers, corresponding to the elongated symmetrized wake. The effect is quantified by average turbulence intensity for a given streamwise location  $\langle TI \rangle_{x^*}$  presented in figure 11(c). As observed, the average fluctuation within the shear layers increase in a linear manner along the length of the recirculation region achieving a maxima well before the bubble closure. On average, the  $C_q^{lo}$  case presents similar levels of fluctuations up to  $x^* \approx 0.6$ , beyond which the maximum values are reduced. On the other hand, the  $C_q^{opt}$  blowing results in a decrease of slope  $d\langle TI \rangle_{x^*}/dx^*$  with significant reductions in turbulent fluctuations along the whole length of the recirculation region. It is pertinent to mention that these changes are isolated to within the separated shear layers and do not represent the turbulent fluctuations within the inner recirculation region, where the optimal injection flow is bound to introduce added turbulence close to the longitudinal axis of the wake.

The modifications of the separated shear layers described above imply that their entrainment capacity is also modified. The entrainment of the shear layers before roll-up is one of the key ingredients that determines the recirculation region size and shape, and in the following we will assess its consequences. A simple flow rate budget across the shear layer gives  $V_E dx = U_c d\delta$  (Lorite-Díez *et al.* 2020b), where  $V_E$  is the entrainment velocity and  $U_c$  is the convective velocity within the shear layer. We evaluate the non-dimensional entrainment velocity on the SLI using

$$V_E^* = u_c^* \frac{d\delta^*}{dx^*}, \tag{4.5}$$

hence,  $u_c^* = 0.5$ .

The growth rate for a free mixing layer is characterized in terms of momentum thickness (Dandois, Garnier & Sagaut 2007), which appears in generalized form as

$$\delta_\theta^*(x^*) = \int_{y_{min}^*}^{\infty} \frac{u^*(x^*, y^*) - u_{min}^*(x^*)}{U_\infty^*(x^*) - u_{min}^*(x^*)} \left( 1 - \frac{u^*(x^*, y^*) - u_{min}^*(x^*)}{U_\infty^*(x^*) - u_{min}^*(x^*)} \right) dy^*, \tag{4.6}$$

where  $u_{min}^*(x^*)$  is the local minimum streamwise velocity. Since we are dealing with a complex 3-D flow where  $u_{min}^*(x^*)$  on the inner side of each shear layer is influenced by the recirculating flow from all the other sides and the base blowing (where applicable), we make use of a slightly modified approach. The thickness of the shear layer at each point is obtained by locating the streamwise velocity of  $u^* = 0.4$  and  $u^* = 0.6$  respectively below and above the SLI surface in the direction normal to it. This would be equivalent to finding the momentum thickness between the limits  $U_\infty^* = 0.6$  and  $u_{min}^*(x^*) = 0.4$  in (4.6). The distance between these locations gives the local shear layer thickness as

$$\delta_\theta^* = \langle \sqrt{(\Delta x^*)^2 + (\Delta y^*)^2 + (\Delta z^*)^2} \rangle_{0.4 \leq u^* \leq 0.6} \tag{4.7}$$

Figure 12 shows the distribution of  $\delta_\theta^*$  obtained along the SLI for the three configurations. For all cases, we observe a progressively increasing thickness of the shear layers along the streamwise direction. An asymmetric distribution can be observed for  $C_q^0$  corresponding to the  $N$ -state wake, whereas a downstream shift in the distribution can be discerned for the  $C_q^{opt}$  case indicating a reduced growth rate  $d\delta_\theta^*/dx^*$ . Moreover, higher values of  $\delta_\theta^*$  are also observed along the corners of the SLI. These regions represent the interactions of the shear layers around the corners of the base, which promotes additional mixing resulting in subsequently higher growth rates.

Equilibrium of fluxes in the wake of a 3-D bluff body

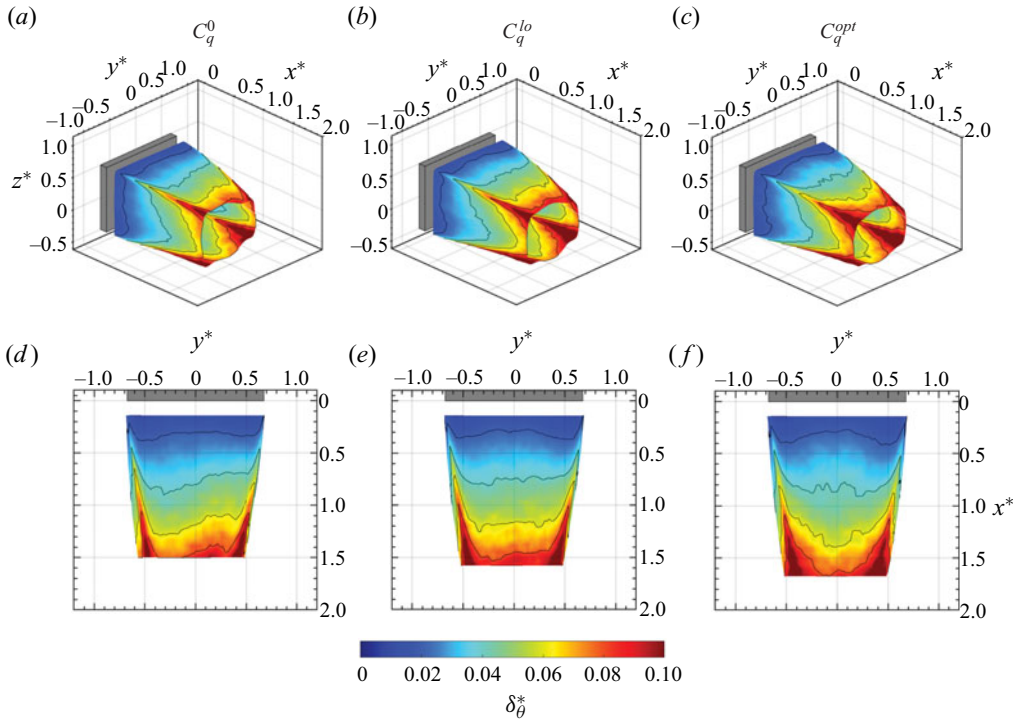


Figure 12. Distribution of shear layer thickness  $\delta_\theta^*$  on the SLI for different flow configurations. Isolines shown for each major colourbar division.

The entrainment flux through the shear layer surface is then calculated as:

$$\Phi_b = \iint V_E^* ds^* dt^*, \quad (4.8)$$

where  $ds^*$  and  $dt^*$  represent the SLI discretized along the cross-sectional perimeter and along the length, respectively. We establish a framework to identify an effective area on the SLI over which flux  $\Phi_b$  of the balance (4.1) will be accounted for. Assigning a constant streamwise length to cutoff this surface will be a crude approximation, since we are not dealing with an isolated planar shear layer. Depending on the state of the wake along with subsequent effect of blowing, the shear layers will evolve at different growth rates around the perimeter of the base before eventually resulting in the closure dynamics of the recirculation region. This effect can be identified by tracking a constant value of  $\delta_\theta^*$ , since variable growth rates will result in achieving this thickness at different downstream locations along the perimeter of the SLI (see, for example, isolines in figures 12). To identify the effective entrainment length over which the shear layer behaves as a canonical mixing layer, we make use of vorticity thickness defined in generalized form as

$$\delta_\omega^*(x^*) = \frac{U_\infty^*(x^*) - u_{min}^*(x^*)}{(\partial u^*(x^*, y^*)/\partial y^*)_{max}}. \quad (4.9)$$

Similar to the predicament of using (4.6) for present shear layers, we apply an alternative approach of evaluating the vorticity thickness. For each streamwise location, the value of  $(\partial u^*/\partial y^*)_{max}$  is determined within the shear layer. The vorticity thickness is evaluated as the distance between the locations on either side of the maximum shear where

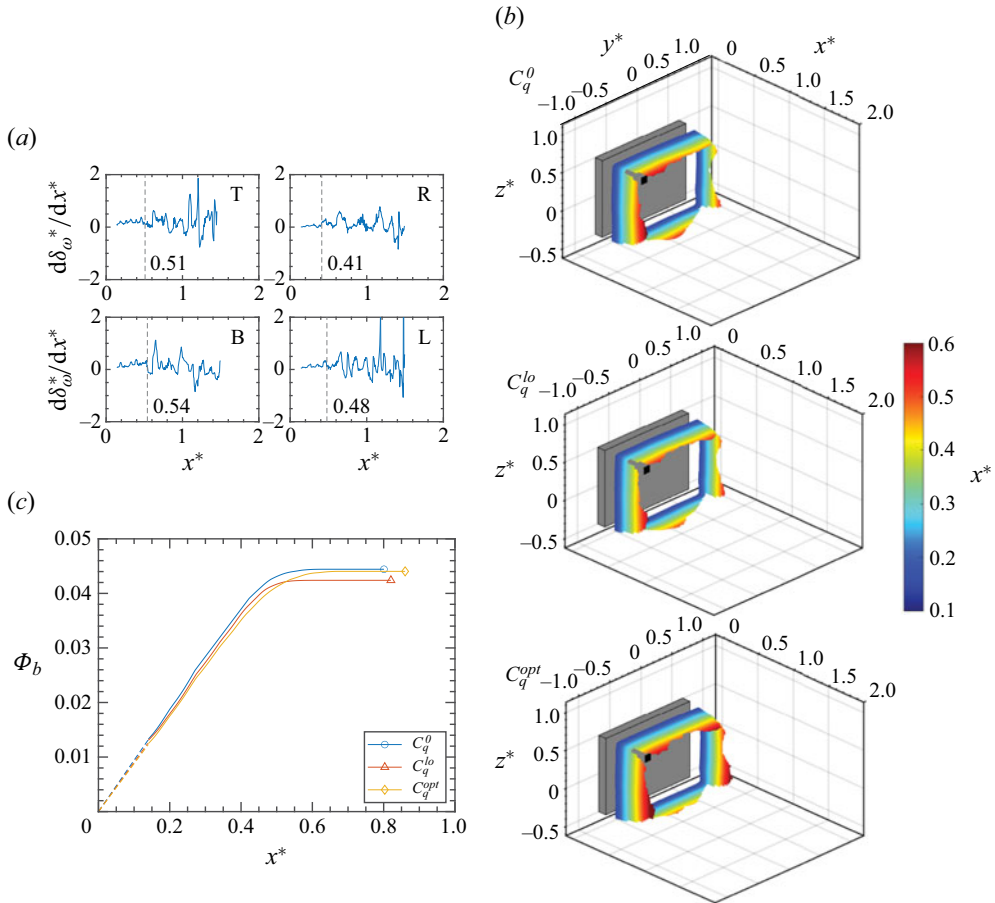


Figure 13. (a) Evolution of vorticity thickness growth rate  $d\delta_{\omega}^*/dx^*$  at centreline locations of the top (T), bottom (B), right (R) and left (L) shear layers for the  $C_q^{lo}$  case. (b) Effective SLI obtained by delimiting the surface based on  $\delta_{\theta}^* = 0.0285$  for all configurations. The surface is coloured by  $x^*$  indicating variable streamwise lengths over which  $\delta_{\theta}^*$  is achieved. (c) Integral of the entrainment flux ( $\Phi_b$ ) over the effective SLI as a function of streamwise location for respective flow rates.

$0.5(du^*/dn^*)_{max}$  is achieved. This treatment is carried out at four distinct centreline locations; the top (T) and the bottom (B) shear layers at the  $y^* = 0$  plane, and the right (R) and left (L) shear layers at the  $z^* = 0$  plane. The results are analysed in terms of vorticity thickness growth rate  $d\delta_{\omega}^*/dx^*$  as shown for the  $C_q^{lo}$  case in figure 13(a). The vertical dashed lines indicate the streamwise locations beyond which the growth rates of the various shear layers start to fluctuate substantially, and the shear layer behaviour deviates from a canonical planar shear layer. In all examined cases, this change in the growth rate behaviour occurs roughly when the thickness achieved is around  $\delta_{\theta}^* = 0.0285 \pm 0.0019$ . Thus, we will use this common  $\delta_{\theta}^* = 0.0285$  as a threshold value beyond which the shear layer cannot be considered anymore to contribute to  $\Phi_b$  as predicted by the entrainment velocity model.

Figure 13(b) shows the resulting SLI delimited by  $\delta_{\theta}^* = 0.0285$ , where the surface is coloured by the streamwise location  $x^*$  at which the threshold thickness is achieved. For  $C_q^{lo}$ , we can observe the main effect to be that of symmetrization where a decrease in



## Equilibrium of fluxes in the wake of a 3-D bluff body

Case	$\Phi_a$	$\Delta_a$	$\Phi_b$	$\Delta_b$	$\Phi_c$	$\Delta_c$	$\Phi_q$
$C_q^0$	0.1083	—	0.0444	—	0.1527	—	0
$C_q^{lo}$	0.0971	−10.4 %	0.0424	−4.5 %	0.1359	−11 %	0.0036
$C_q^{opt}$	0.0623	−42.5 %	0.0440	−0.9 %	0.0991	−35.1 %	0.0072

Table 2. Values of fluxes  $\Phi$  obtained for the budget of (4.1) for respective flow rates  $C_q$ . The percentage relative change in each flux with respect to the baseline value at  $C_q^0$  is presented as  $\Delta = [(\Phi(C_q) - \Phi(C_q^0))/\Phi(C_q^0)] \times 100$ .

the length of the left side shear layer is accompanied by an increase in the length of the right side. The effect is also visible through symmetrization of the top shear layer surface when compared with the  $C_q^0$  case. For the  $C_q^{opt}$  case, the main effect appears to be in the form of elongation of the recirculation region that is evidenced by an increased length of the effective SLI. Apart from the reduction in the expected asymmetric conformity of the surface with base blowing, we can observe a discontinuity around the top corners of the SLI that is attributed to the higher thickness value in this region as discussed earlier (see figure 12). The effect is more dominant near the bottom corners, which is indicated by the diminishing bottom surface away from the axis of symmetry. This may be attributed to the circular mounting struts that promote increased growth rates in the separating shear layers. The entrainment over this reduced surface is then estimated using (4.8) to obtain an integral of flux  $\Phi_b$  in the streamwise direction, as shown in figure 13(c). The curves saturate for respective cases based on the diminishing contribution of the shear layer surface beyond the cutoff region. The dashed portion of the curves indicates a linear fit applied on the early part of the integral  $\Phi_b$  to account for the missing PIV data near the base. The goodness of the fit is evaluated based on minimizing the norm of residuals for each case. Compared with  $C_q^0$ , the  $C_q^{lo}$  and  $C_q^{hi}$  cases evolve with slightly different slopes depending upon the entrainment capacity of the shear layers evaluated over the effective SLI. Interestingly, the total  $\Phi_b$  value for  $C_q^{lo}$  is slightly smaller, while  $\Phi_b$  for  $C_q^{opt}$  is almost identical to the  $C_q^0$  case. As done for the flux  $\Phi_c$ , a convergence check on flux  $\Phi_b$  estimation is also carried out for the last 100 PIV snapshots that gives a standard deviation  $\sigma(\Phi_b) = 1.1 \times 10^{-5}$ .

### 4.4. Flux balance and flow regimes

We now examine the variations in different fluxes for each flow configuration. The values of fluxes are presented in table 2, where  $\Phi_b$  and  $\Phi_c$  are obtained from §§ 4.3 and 4.2, respectively,  $\Phi_a$  is obtained as a consequence of the balance (4.1) and base blowing flux is obtained as  $\Phi_q = q_j/U_\infty H^2$ . For each blowing case, table 2 also shows the percentage relative change ( $\Delta$ ) in each flux compared with the respective baseline values at  $C_q^0$ . Continuing from our analysis of shear layer entrainment in § 4.3, we first address the variations for flux  $\Phi_b$ . For  $C_q^{lo}$ , a reduction of 4.5 % is observed compared with the  $C_q^0$  case. For  $C_q^{opt}$ , we attain similar values of  $\Phi_b$  with a negligible reduction of 0.9 %. On the other hand, considerable changes in the replenishment influx are observed; from table 2 we note a reduction of  $\Phi_c$  of 11 % for  $C_q^{lo}$  and 35.1 % for  $C_q^{opt}$ . We may expect  $\Phi_a$  to behave similarly to  $\Phi_c$ , since both fluxes are generally related to the roll-up dynamics of

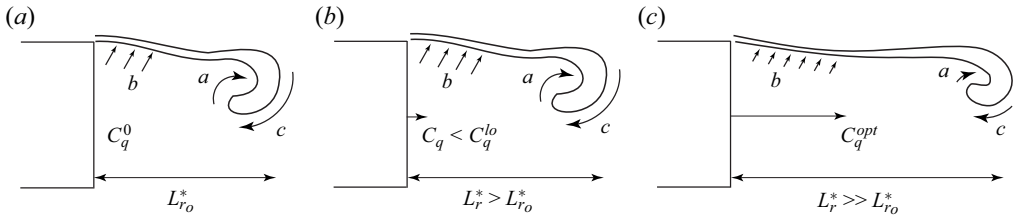


Figure 14. Conceptual sketches of the (a) natural wake and the drag reduction mechanism through centralized base blowing under the (b) mass regime and (c) favourable momentum regime. Balance between different fluxes of the budget (4.1); fluxes feeding the recirculation region as induced replenishment flow ‘c’ by vortex roll-up and through base blowing ‘ $C_q$ ’, whereas fluxes emptying the recirculation region through fluid engulfment ‘a’ of the shed vortex as well as the entrainment ‘b’ of the shear layers.

the bubble closure mechanism (Lorite-Díez *et al.* 2020b). For  $C_q^{lo}$ , this is the case as the  $\Phi_a$  is also reduced by 10.4 %. For  $C_q^{opt}$ , we observe a much greater reduction of  $\Phi_a$  by 42.5 %. The latter reduction here is obtained from the balance of fluxes but is also consistent with the partially measured  $\Phi_{a+b}$  as shown in table 1 earlier. In the following we discuss the mechanisms through which the recirculation region and drag are modified based on the observed variations of fluxes, as illustrated in figure 14.

The unactuated wake (figure 14a) presents a balance between the replenishment influx  $\Phi_c$  that feeds the recirculation region, and the extraction of fluid from this region through the entrainment flux  $\Phi_b$  along the length of shear layers and through the engulfment flux  $\Phi_a$  of vortices being shed downstream. The asymmetry of the unactuated wake provides a strong bias of the replenishment flux in the direction of bistable state switching. From figure 7(b) it is evident that the side of the wake featuring the low-pressure, large recirculating vortex close to the base ( $y^* > 0$  for the  $N$ -state wake) is responsible for providing a major part of this influx. By splitting the total  $\Phi_c$  across the RRI using a vertical plane orthogonal to the base and containing the stagnation point in the wake for the conditionally averaged  $N$  state, we obtain a contribution of 20 % and 80 % respectively between the left and right sides of the wake.

Drag reduction first occurs with a very low momentum base blowing ( $C_q < C_q^{lo}$ ), where the injected flow acts as a passive scalar in the ‘mass regime’, as illustrated in figure 14(b). In this regime, as proposed by Lorite-Díez *et al.* (2020b), the momentum of the added flux  $\Phi_q$  is dissipated in the recirculation region, and the fluxes  $\Phi_a$  and  $\Phi_c$  remain unchanged. As a consequence, the added flux  $\Phi_q$  is compensated by the entrainment flux  $\Phi_b$  acting over a longer length of the slightly enlarged recirculation bubble ( $L_r^* > L_{r0}^*$ ). In the current experiment this regime is identified for the initial two data points (see data in figure 3a) marked as region ‘I’ in figure 15(a). The identifying characteristic of the mass regime is the affine relationship of  $C_B$  vs  $C_q$ , as observed in the experiments of Bearman (1967) and Lorite-Díez *et al.* (2020b) for the 2-D and 3-D bluff bodies, respectively. Although these blowing rates were not examined using PIV in the current experiment, we can use the available data from table 2 to assess that the magnitude of the injected flux for  $C_q < C_q^{lo}$  would be a significantly smaller quantity compared with  $\Phi_b$  (an order of magnitude smaller) and, hence, would require a very small increase in  $L_r^*$  to compensate for this additional flux. This effect can be seen through figure 15(b), where the dashed line represents the linear relationship between  $\Delta C_B$  and  $\Delta L_r^*$  in the mass regime for perimeteric base blowing of Lorite-Díez *et al.* (2020b). The data pertaining to the mass regime in the current experiment is predicted on the slope based on the available  $\Delta C_B$  information.

Equilibrium of fluxes in the wake of a 3-D bluff body

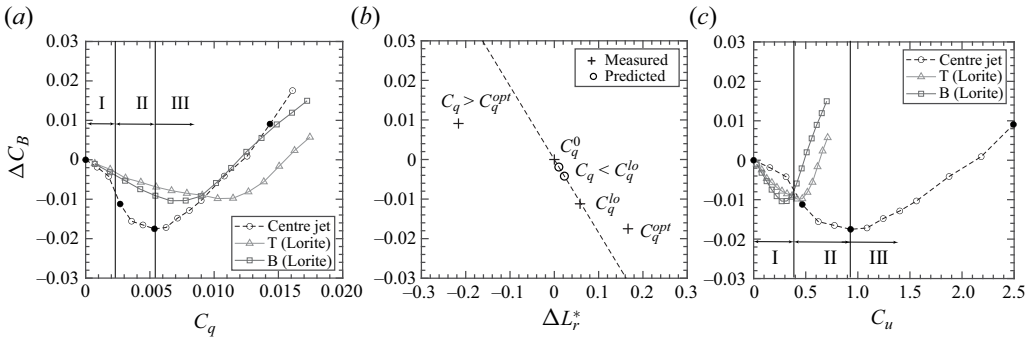


Figure 15. Changes in base suction coefficient ( $\Delta C_B$ ) with (a) blowing coefficient  $C_q$ , (b) changes in recirculation region length ( $\Delta L_r^* = L_r^* - L_{r0}^*$ ) and (c) momentum coefficient  $C_u$ . The filled markers correspond to  $C_q^{PIV}$ . The extent of the mass regime (I), the favourable momentum regime (II) and the momentum regime (III) for the present study are highlighted. Results of steady blowing from the top (T) and bottom (B) slit are shown from Lorite-Díez *et al.* (2020b). Dashed line in (b) depicts a linear relationship  $\Delta C_B = -0.185\Delta L_r^*$  observed for drag reduction in the mass regime of Lorite-Díez *et al.* (2020b).

It is clearly evident that the change in  $\Delta L_r^*$  caused for  $C_q < C_q^{lo}$  is significantly smaller compared with the flow rates examined through PIV measurements in the present study.

At higher blowing rates of the actuator, a substantial drag reduction is accomplished by completely different dynamics illustrated in figure 14(c); an example of which would be  $C_q^{opt}$  in the current experiment. In this regime the recirculation bubble length is significantly increased, delaying and weakening the bubble closure dynamics. As a consequence, fluxes  $\Phi_a$  and  $\Phi_c$  are much reduced as noted in table 2. This case appears as a deviation from the linear  $\Delta C_B$  vs  $\Delta L_r^*$  relationship, featuring a much larger increase in recirculation region length, evidenced in figure 15(b). Although the magnitude of added flux  $\Phi_q$  is very small compared with the reduction in  $\Phi_c$ , its momentum appears to be able to significantly counteract the reverse wake flow. The momentum effect is clearly evident from the downstream extent of the jet signature in the recirculation region (see figure 6), as well as from the relationship between the  $\Delta C_B$  and the momentum coefficient  $C_u$  in figure 15(c). For example, when the flow rate from  $C_q^{lo}$  to  $C_q^{opt}$  is increased by a factor of 2, the jet velocity almost reaches the magnitude of  $U_\infty$ . It is evident that the mean recirculation bubble modifications in this case clearly are a consequence of momentum; thus, we propose to refer to this mechanism as the ‘favourable momentum regime’ in light of the favourable drag reduction effect. The enhanced drag reduction effect can be seen through region ‘II’ in figure 15(a) with the  $C_q^{opt}$  case marking the end of this regime. We can note that this regime is reminiscent of the mid-shear configuration presented in Parezanović & Cadot (2012) for a 2-D cylinder, where a smaller control cylinder is placed in its wake in such a way to partially deflect the free-stream momentum into the wake. As in the current experiment, the recirculation bubble is enlarged but remains intact, accompanied by a significant drag reduction and a strong damping of the global mode. As for the shear layer entrainment flux  $\Phi_b$ , the growth of the shear layers is reduced by the modified dynamics of the recirculation bubble, which decreases their entrainment capacity, as evident by the decreased turbulent fluctuations in figure 11(c). However, this reduced entrainment now acts over the increased length of the recirculation bubble and yields a  $\Phi_b$  very similar to the unactuated flow (see table 2). The reduced entrainment of the shear layers per unit length (or rather unit surface area in the 3-D wake) is to be expected if the

shear layers are to be delayed in their roll-up and mutual interaction, as is the case for the elongated recirculation region.

At the threshold between the two regimes previously described, we find the  $C_q^{lo}$  case. For  $C_q^{lo}$ , we indeed observe that the shear layers initially have, on average, similar turbulent characteristics as the natural wake up to  $x^* \approx 0.6$ , as shown in [figure 11\(c\)](#). Moreover, from [figure 15\(b\)](#), we see that  $C_q^{lo}$  lies on the slope of the mass regime, albeit with both  $\Delta L_r^*$  and  $\Delta C_B$  greatly increased compared with the preceding lower flow rates. This observation also gives confidence on the predicted placement of the lower flow rates on the mass regime slope. On the other hand, the  $C_q^{lo}$  case also indicates a change in the wake regime since the large  $\Delta C_B$  is no longer following the linear increase in  $C_q$ . The  $C_q^{lo}$  case exhibits a relatively high momentum coefficient (see [figure 15c](#)) compared with the top and bottom blowing in Lorite-Díez *et al.* (2020b), although the jet is barely visible in the mean flow fields of [figure 6](#). As mentioned earlier and detailed in [table 2](#), both  $\Phi_b$  and  $\Phi_c$  fluxes are modified and their changes do not correspond to the expected behaviour for the mass regime. Finally, from the time series of pressure gradients in [figure 4\(a\)](#) we can see that the asymmetry of the wake still exists, although with a smaller maximum amplitude and much more frequent exchanges between the two states. This brings us to the conclusion that  $C_q^{lo}$  is a transitional regime, leading to the favourable momentum regime. The emerging symmetrization may be contributing positively to drag reduction (Haffner *et al.* 2021; Keirsbulck *et al.* 2023), and the momentum of actuation starts to affect the wake fluxes.

The region marked as ‘III’ in [figure 15\(a,c\)](#) denotes the ‘momentum regime’ and extends for flow rates beyond  $C_q^{opt}$ . This regime is associated with adverse effects of blowing momentum that results in an increased drag configuration. The  $C_q^{hi}$  case for the present blowing would be an example of this regime, where the blown jet acts to split the recirculation region (see [figure 6](#)), and the conventional wake is replaced by a toroidal topology of the recirculation bubble. Although the flux analyses discussed above could (possibly) still be applied, the departure from a canonical wake is so large that analysis would not provide any further insight into the physics of bluff body wakes.

In comparison with the top and bottom blowing from Lorite-Díez *et al.* (2020b), central injection can be performed with a much larger momentum before adverse effects are observed, as can be seen from [figure 15\(c\)](#). Although the middle of the recirculation bubble is not a typical target for flow control since its low momentum dynamics is not sensitive to perturbations, it is an advantageous location for enlarging the bubble by mass addition precisely due to its lack of sensitivity to the momentum of the actuator jet. Despite the momentum of our actuation at  $C_q^{opt}$  being so much higher, the added mass itself is lower than in the cases of the top and bottom blowing. Had the central blowing in the current experiment been implemented through a larger orifice (thus, a lower momentum) we could expect the adverse effects of momentum regime to be triggered at a higher  $C_q$ , which would reduce the drag even more. Similar results have been observed for the 2-D bluff body in the experiments by Wood (1964) and Bearman (1967) using different surface areas for base bleed.

Finally, for the  $C_q^{lo}$  case in the current experiment, the relative changes compared with the unactuated wake in  $L_r^*$  and  $\Phi_c$  are 4% and –11%, respectively. Taking into account that this case does not qualify as the mass regime but is rather close to it, the question remains whether the replenishment flux  $\Phi_c$  (and thus, the engulfment  $\Phi_a$ ) can remain constant in the mass regime, where an expected change in  $L_r^*$  might be  $\sim 2\%$  possibly implying a  $\Phi_c$  change of around –5%. The methodology presented in this paper should be applied to such a case to verify the model proposed in Lorite-Díez *et al.* (2020b).

## 5. Coherent flow structures

The 3-D description of the flow field is utilized for comprehending the dominant structures in the wake. The POD applied to the complete set of stereoscopic velocity fields, in all the planes, enables us to identify the coherent structures associated with the natural symmetry-breaking states and those resulting from base blowing.

### 5.1. Proper orthogonal decomposition

Any snapshot of the flow field  $V(\mathbf{x}, t)$ , with components  $u(\mathbf{x}, t)$ ,  $v(\mathbf{x}, t)$ ,  $w(\mathbf{x}, t)$ , can be expressed as

$$V(\mathbf{x}, t) = \bar{V}(\mathbf{x}) + V'(\mathbf{x}, t) = \bar{V}(\mathbf{x}) + \sum_{n=1}^{N_s} a_n(t)U_n(\mathbf{x}), \quad (5.1)$$

where  $\bar{V}(\mathbf{x})$  and  $V'(\mathbf{x}, t)$  are respectively the (time-averaged) mean and fluctuating flow fields, and  $\mathbf{x}$  the spatial coordinates. Using POD, we can decompose the fluctuating part of the field variable into a set of POD modes  $U_n(\mathbf{x})$  (also known as spatial functions), with coordinates  $u_n(\mathbf{x})$ ,  $v_n(\mathbf{x})$ ,  $w_n(\mathbf{x})$ , and related temporal coefficients  $a_n(t)$ , where  $N_s$  represents the number of snapshots. The spatial functions are obtained by solving an eigenvalue problem of the covariance matrix

$$C = XX^T, \quad (5.2)$$

where  $X$  is the data matrix containing the spatial and temporal information of the fluctuating field. The obtained eigenvalues,  $\lambda_1 \geq \lambda_2 \geq \dots \geq \lambda_n$ , represent the energy content of the fluctuations associated with each POD mode arranged in a decreasing energy order. The most energetic modes can then be used to identify the most coherent features of the flow field. More details on the description and application of POD to turbulent flows can be seen in Holmes, Lumley & Berkooz (2010) and Weiss (2019).

### 5.2. Modes of the natural wake flow

A visualization of the most dominant modes detected in the wake of the unactuated flow case are presented in figure 16. Here we consider the first three modes ( $n = 1, 2, 3$ ), as they contribute to approximately 22 % of the total energy content of the fluctuating flow field (see figure 17a). The  $u$  component of the first mode  $U_1$  presents two vertical structures with opposite phases lying on either side of the vertical plane of symmetry. The  $v$  component of  $U_1$  appears as a horizontal sandwich structure with an opposite phase in the centre, whereas the  $w$  component of  $U_1$  presents a four node pattern aligned with each corner of the base and having similar phase in diagonal orientation (see figure 16b,c). The resulting streamline patterns are plotted in figure 16(d) using all three components of mode  $U_1$ . As shown, mode 1 is described by two counter-rotating vortices aligned with the horizontal plane and is responsible for introducing the lateral symmetry breaking of the flow. This is consistent with the pattern reported by Pavia *et al.* (2018) for their stereo PIV measurement done on two cross-stream planes, whereas we see in the present study that the mode description for the main contributors ( $v$  and  $w$  components) remain consistent across all the planes for the entire length of the recirculation region. The evolution of the temporal coefficient associated with this mode is shown in figure 17(b), where a clear description of the long-time bistable dynamics of the wake is recovered, confirming that  $U_1$  is associated

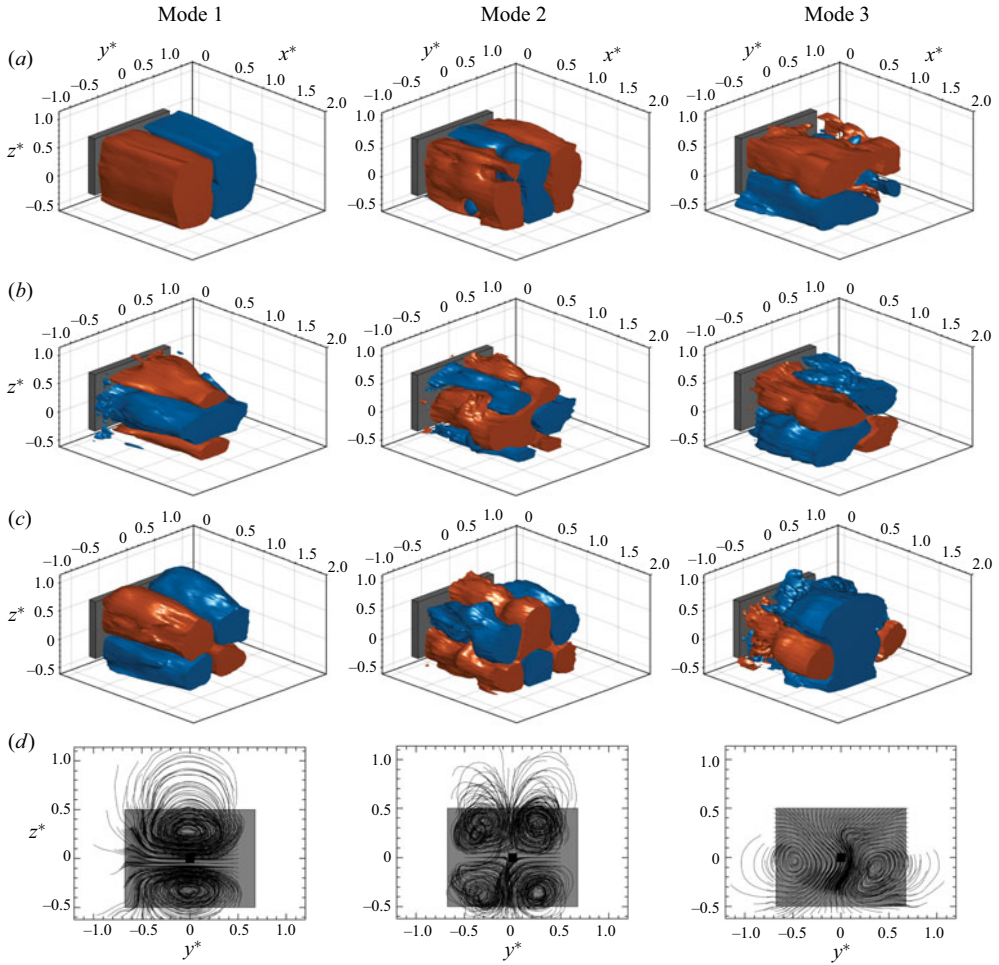


Figure 16. Spatial functions of the first three modes ( $n = 1, 2, 3$ ) extracted from SSPIV data for the unactuated wake. Mode shapes represented as an isosurface of (a) axial  $u_n^*$ , (b) lateral  $v_n^*$  and (c) vertical  $w_n^*$  components of spatial function  $U_n$ . Isosurface values are  $u_n^*, v_n^* = \pm 0.002$  and  $w_n^* = \pm 0.001$ , where red and blue indicate positive and negative values, respectively. (d) Streamline patterns corresponding to each mode drawn using all three components ( $u_n^*, v_n^*, w_n^*$ ) of respective spatial function  $U_n$ .

with the flow structure that breaks the symmetry of the flow. Moreover, we also observe that with base blowing, the temporal coefficient  $a_1(t)$  presents a significantly weakened bistable behaviour in the  $C_q^{lo}$  case and becomes indistinguishable in the  $C_q^{opt}$  case. The effect is also visible in the energy fraction shown in figure 17(a), where the energy content associated with the lateral symmetry-breaking mode decreases by approximately 75% at the optimal blowing, compared with the unactuated flow. Hence, the POD analysis is able to accurately capture the positive effects of centralized base blowing on suppression of the RSB mode.

The POD mode  $U_2$  is formed by a vertical sandwich structure having a similar phase on the outer side, as shown in figure 16. Here, the  $v$  and  $w$  components of mode  $U_2$  present an intersecting ‘C structure’ and ‘V structure’, respectively, that yield a streamline pattern of four counter-rotating vortices. This pattern is associated with a symmetry preserving mode

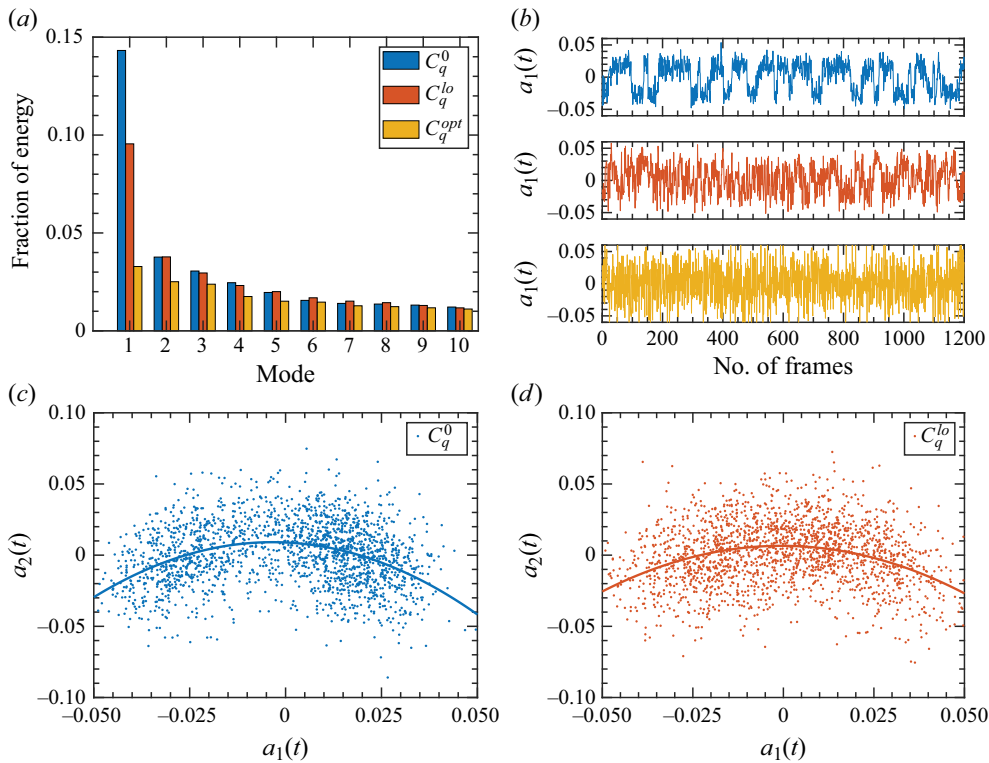


Figure 17. (a) Fraction of energy associated with the first 10 POD modes. (b) Evolution of the first POD mode temporal coefficient for respective flow rates. (c) Scatter plot of temporal coefficients associated with lateral symmetry-breaking mode  $a_1(t)$  and symmetry preserving bubble pumping mode  $a_2(t)$  for respective flow rates. Solid lines represent a curve fit on the data.

that accounts for the longitudinal motion of the wake. As described by Pavia *et al.* (2018), this motion is linked to the pressure variation at the base where a transitional symmetric state, during the wake state switching, results in an elongation of the recirculation region and a concomitant reduction of base drag. Figure 17(d) shows a correlation between the temporal coefficient of the lateral symmetry-breaking mode  $a_1(t)$  and the symmetry preserving mode  $a_2(t)$ . For the unactuated flow, the dominant asymmetric states are visible as a concentration of either positive or negative  $a_1(t)$  values. The maximum values of  $a_2(t)$  are achieved during the transition states when  $a_1(t) \rightarrow 0$ . For the  $C_q^{lo}$  case, the distribution of  $a_1(t)$  merges near the symmetric state whereas the variation of  $a_2(t)$  remains unchanged. The change is consistent with the variation observed in mode energies, where the energy content for mode 1 reduces with no change observed for mode 2.

Finally, the  $u$  component of mode  $U_3$  presents two horizontal structures apart from the horizontal plane. The mode structure in the  $v$  and  $w$  components appear interchanged when compared with mode 1, resulting in streamline patterns of two counter-rotating vortices but aligned with the vertical plane of symmetry. Since the wake does not present a vertical symmetry-breaking mode, this mode is associated with any vertical asymmetry that is induced due to the underbody flow.

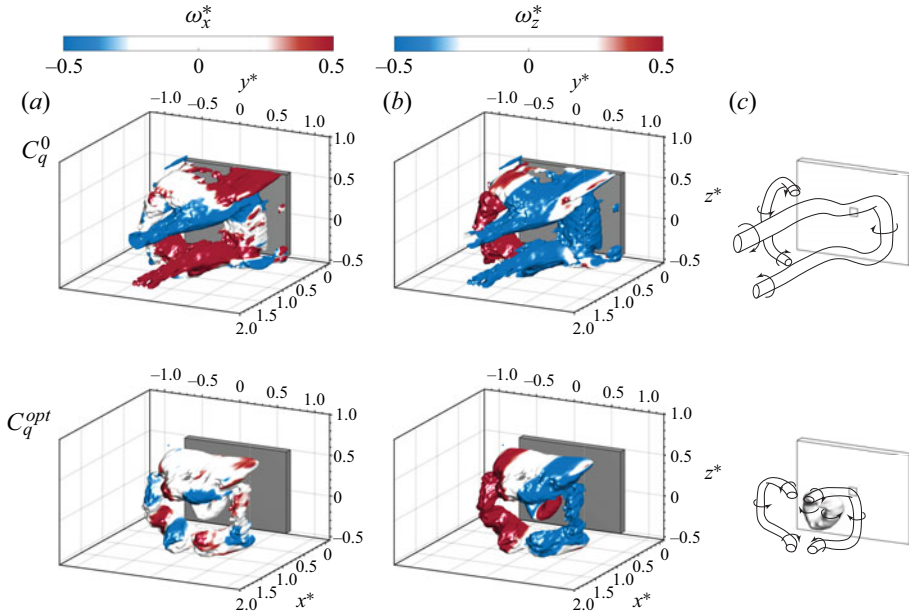


Figure 18. Coherent wake structures for the unactuated flow and optimal blowing case. The structures are visualized through an isosurface of  $Q^* = 0.5$  (Hunt *et al.* 1988), coloured by vorticity ( $\omega^*$ ) components in the (a) longitudinal and (b) vertical direction. Results for the  $N$ -state wake are obtained by combining the ensemble-averaged field with POD mode 1. (c) Sketch representing the dominant structures in the wake for both cases.

### 5.3. Flow structures in the wake

The coherent structures associated with the symmetry-breaking state are extracted using the POD mode descriptions discussed above. Following Thacker *et al.* (2010) and Perry *et al.* (2016), a lower-order model of the flow field can be constructed as

$$\mathbf{V}(\mathbf{x}, t) \approx \bar{\mathbf{V}}(\mathbf{x}) + \sum_{n=1}^{N_m} a_n(t) \mathbf{U}_n(\mathbf{x}), \quad (5.3)$$

where  $N_m$  is the cutoff for the number of modes used to distinguish between coherent and incoherent flow fields. Here  $N_m = 1$  in order to identify the most coherent features of the lateral symmetry-breaking mode. We make use of the condition  $a_1(t) < 0$  to isolate the structures associated with one of the asymmetric states, the other being mirror symmetric. Figure 18 shows the prominent flow features of the unactuated and the actuated wake using the  $Q$  criterion of Hunt, Wray & Moin (1988). The  $Q$  criterion is computed using  $Q^* = \frac{1}{2} [|\Omega^*|^2 - |S^*|^2]$ , where  $\Omega^*$  is the rotation tensor and  $S^*$  the rate of strain tensor,  $|\cdot|$  representing the trace of the tensor. Here  $Q^* > 0$  identifies areas in the wake flow where rotational motion is dominant, indicating the location of main vortex structures.

#### 5.3.1. Natural flow structure

Figure 18 shows structures corresponding to the  $N$  state of the unactuated wake obtained as the isosurface of  $Q^* = 0.5$ . We observe the presence of two horseshoe structures that emanate from the vertical edges of the base. The core of the right-side structure appears closer to the base and is associated with the larger recirculation of the asymmetric



wake, whereas the core of the left-side structure is located farther downstream. Another prominent feature appears as two vortical structures propagating in the longitudinal direction. The isosurface in [figure 18\(a\)](#) is coloured by the distribution of vorticity in the streamwise direction ( $\omega_x^*$ ). By looking at the continuity of the vorticity, it becomes evident that these structures connect to the horseshoe vortex that is located closer to the base. This observation is consistent with the findings of Pavia *et al.* (2020), who describes these structures are tails of a hairpin vortex. They observed that the top tail formation mostly prevails over the bottom one, whereas in the present study we observe both tails of this hairpin vortex to be well formed. [Figure 18\(b\)](#) shows the distribution of vorticity ( $\omega_z^*$ ) along the vertical direction on the same surface. The distribution separates the structures as per the two recirculations in the horizontal orientation. The structure on the left side of the base is then described by a ‘C’-shaped horseshoe vortex that seems to interact with the hairpin vortex from the opposite side. The two structures corresponding to the  $N$ -state wake are sketched in [figure 18\(c\)](#). It is then proposed that the tails of the stronger hairpin vortex interacts with the tails of the opposite ‘C’-shaped vortex. The former, having greater vorticity, overcomes the weaker vorticity of the latter, limiting its formation in the streamwise direction. As a result, the hairpin structure pinches off the ‘C’-shaped vortex and travels downstream.

### 5.3.2. *Optimal blowing flow structure*

The wake structures for the optimal blowing case are obtained from the ensemble-averaged flow as the energy associated with mode 1 is considerably reduced, making it indistinguishable from successive modes, whereas the time coefficient  $a_1(t)$  trend also presents diminished wake bistability, as shown in [figure 17](#).

Based on the same  $Q$  criterion, the wake now presents symmetrized structures parallel to the base. The main features are described by the same horseshoe vortex from each side of the base, shifted farther downstream in tandem. An interesting observation is the presence of two tails on either side of the vertical plane of symmetry, which are identified by opposing longitudinal vorticity ( $\omega_x^*$ ) as shown in [figure 18\(a\)](#). The structure formed due to base blowing is also visible as a torus at the centre of the base and presents an opposing vorticity to the horseshoe vortex, as identified by the  $\omega_z^*$  distribution in [figure 18\(b\)](#). The mechanism of wake symmetrization is then proposed as follows: the opposing vorticity of the blown jet first affects the vortical structure that is closer to the base. As a result, the dominant hairpin vortex on the right side decreases in strength and moves away from the base. Concomitantly, the tails of the hairpin vortex are also weakened and now attain a balance with the tails of the horseshoe vortex on the left. The equal and opposing vorticity interaction between the tails of the two structures annihilate each other and do not propagate downstream. As shown in [figure 18\(c\)](#), the resulting structures are a pair of ‘C’-shaped horseshoe vortices parallel to the base, which may coalesce to resemble a toroidal structure.

### 5.3.3. *Reynolds stress*

The effect of blowing on the wake structures described above is linked to the changes in stress distribution. [Figure 19](#) shows the Reynolds shear stress ( $u^*v^*$ ) in the horizontal  $y^* = 0$  plane for drag reducing cases.

For  $C_q^0$ , we observe an asymmetric distribution with high levels of stress in the left-side shear layer opposite to the large recirculation. The distribution may be indicative of the shear layer triggering mechanism as proposed by Haffner *et al.* (2020). They propose a

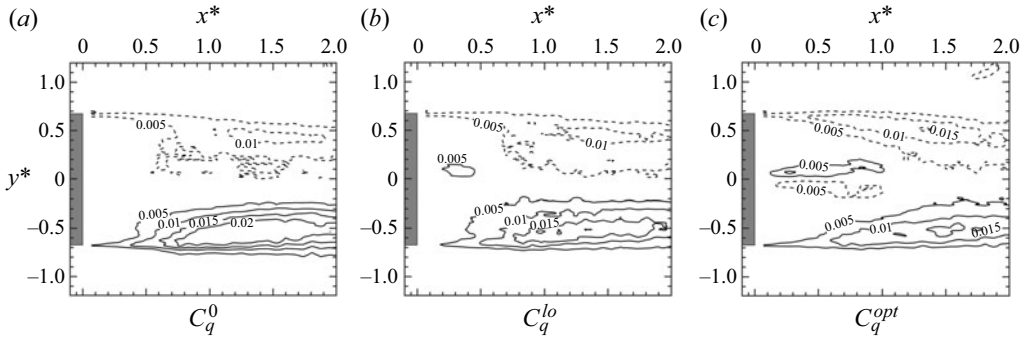


Figure 19. Contours of Reynolds shear stress ( $u^*v^*$ ) distribution on the horizontal  $y^* = 0$  plane for respective flow rates. All distributions are shown for the  $N$ -state sampled wake. Solid and dashed lines represent the positive and negative stress values, respectively, in the range  $\pm 0.02$ .

precursor event, where the feedback from the curved shear layer interacts with the opposite shear layer, promoting roll-up. This leads to an increased engulfment in the recirculation region and, along with sufficient momentum exchange in the wake, results in wake state switching.

For the  $C_q^{lo}$  case, we show the starting effect of base blowing. As proposed in § 5.3.2, the opposing vorticity of the jet starts to weaken the hairpin vortex close to the base on the right side. This translates to a decreased recirculation and subsequently a reduced feedback flow to the opposite shear layer. Such low momentum centralized base blowing is less likely to result in any direct interaction with the separated shear layers. A considerable reduction of stress in the left shear layer is then attributed to the changing curvature of the feedback flow that inhibits triggering interactions. This leads to decreased engulfment potential, which eventually translates in subdued bistability.

As for the extreme case of  $C_q^{opt}$ , the jet acts to bifurcate the feedback flow completely, as also seen in figure 6. A balanced distribution is observed in both shear layers with no triggering precursors for bistability. Moreover, significant fluctuations are introduced by the jet close to the base that, along with the low pressure induced by the jet, limits the gain in drag reduction and explains the flattening of the drag reduction curve around  $C_q^{opt}$ .

## 6. Blowing under side-slip conditions

Ground transport vehicles may often encounter free-stream flow with some side-slip conditions. Compared with the mirrored asymmetric states introduced by bistability, the wake under side-slip conditions is locked towards one side and the level of asymmetry depends upon the amount of side slip experienced by the body. In this section we analyse the benefits of centralized steady jet base blowing on the Ahmed body wake resulting from an asymmetric free-stream flow.

### 6.1. Drag and wake asymmetry

The effect on drag reduction for the case of  $\beta = 5^\circ$  is presented in figure 20(a). The baseline values are found to be  $C_{B_0} = 0.2274$  and an axial force coefficient  $C_{x_0} = 0.4471$  (an increase of 27% and 19%, respectively, compared with  $\beta = 0^\circ$ ). As the blowing coefficient is increased, the values of  $C_B$  and  $C_x$  gradually decrease to a minimum at a slightly higher  $C_q^{opt} = 0.0063$ , where the base suction and drag coefficients are decreased

## Equilibrium of fluxes in the wake of a 3-D bluff body

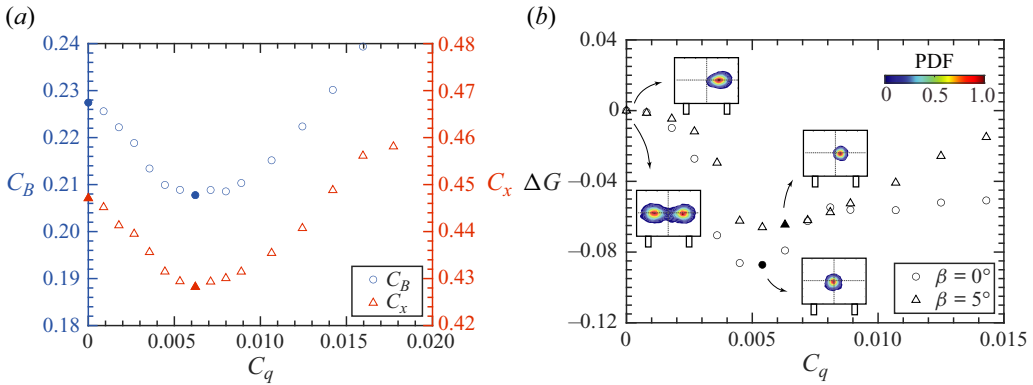


Figure 20. (a) Effect of base blowing on base suction coefficient ( $C_B$ ) and drag coefficient ( $C_x$ ) for  $\beta = 5^\circ$ . The filled markers correspond to  $C_q^{PIV}$ . (b) Changes in wake asymmetry strength  $\Delta G$  for  $\beta = 0^\circ$  and  $\beta = 5^\circ$  cases. Filled markers denote  $C_q^{opt}$  for respective cases. Inset shows the joint PDF of the horizontal ( $g_y$ ) and vertical ( $g_z$ ) pressure gradient at the base for  $C_q^0$  and  $C_q^{opt}$  cases.

by around 8 % and 4 %, respectively. The effect of base blowing on the asymmetry induced due to bistability for the  $\beta = 0^\circ$  case and due to side slip for the  $\beta = 5^\circ$  case is compared in terms of the wake asymmetry strength  $G = \sqrt{g_y^2 + g_z^2}$ . Figure 20(b) presents the changes to the asymmetry strength as  $\Delta G = G - G_0$ . For  $\beta = 0^\circ$ , we observe a significant reduction of  $G$  with a minimum value achieved at  $C_q^{opt}$ , which is an effect of a perfectly symmetrized wake as seen before. Interestingly, the effect of transition from the mass regime to the favourable momentum regime is also visible in terms of a sudden decrease in the wake asymmetry strength, which also contributes to the sudden decrease of drag observed for this case. For increased flow rates, the wake maintains an asymmetry strength lower than the natural flow state. A similar effect is observed for blowing at  $\beta = 5^\circ$ , indicating a positive impact towards reducing the wake asymmetry enforced due to side slip. However, the effect is subdued in terms of the maximum asymmetry suppression compared with the  $\beta = 0^\circ$  case. Moreover, increasing the flow rate results in a gradual increase of  $G$  to values closer to the unactuated flow state of  $\beta = 5^\circ$ . The insets in figure 20(b) show the joint probability density functions (PDF) of the horizontal ( $g_y$ ) and vertical ( $g_z$ ) pressure gradients at the base for select flow rates. For  $\beta = 0^\circ$ , the unactuated flow presents a bimodal distribution corresponding to the RSB mode, which transitions to a compact unimodal distribution centred at the base for  $C_q^{opt}$ , indicating a perfectly symmetrized wake. For  $\beta = 5^\circ$ , the PDF for the unactuated flow shows no bistability, rather an ellipsoidal distribution is obtained that is shifted towards the right side of the base. With base blowing, the distribution contracts to a unimodal distribution at  $C_q^{opt}$ , moving closer to the centre of the base (albeit not perfectly centred as observed for the  $\beta = 0^\circ$  case).

### 6.2. Wake topology

The SSPIV measurements are also conducted for the unactuated wake and optimal blowing cases (highlighted markers in figure 20a). For  $C_q^0$ , the 3-D recirculation bubble appears significantly skewed towards the right side under the influence of side-slip conditions, as shown in figure 21(a). Compared with the  $\beta = 0^\circ$  case, the maximum length of the

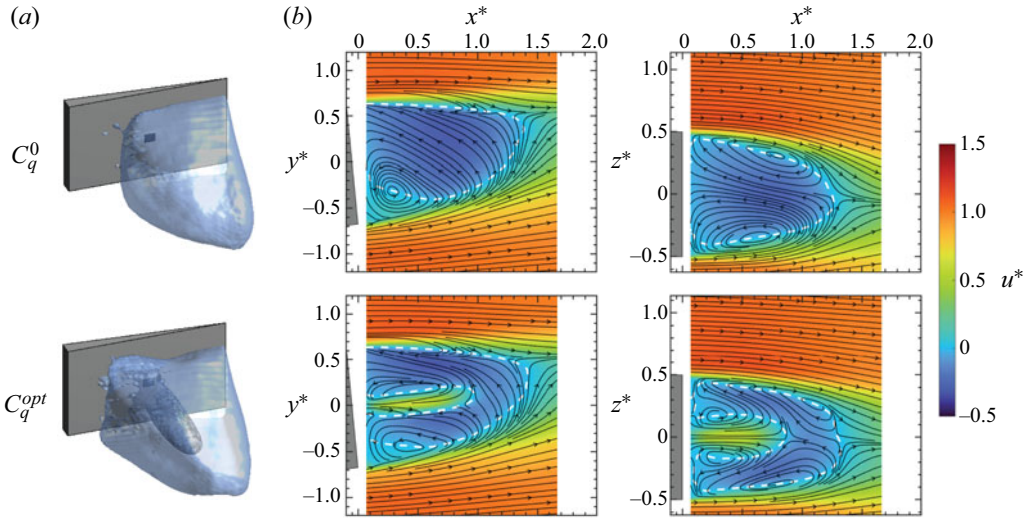


Figure 21. Mean field results for the unactuated flow and optimal blowing at side slip  $\beta = 5^\circ$ . (a) Three-dimensional recirculation bubble visualized through the isosurface of  $u^* = 0$ . The darker shade surface indicates the jet confined within the main recirculation bubble. (b) Streamwise velocity distribution at  $z^* = 0$  and  $y^* = 0$  planes. Ensemble-averaged streamlines are overlaid and the white dashed line represents the recirculation bubble as an isoline of  $u^* = 0$ .

recirculation bubble is reduced with  $L_r^* = 1.41$ , which contributes to a higher base drag. The corresponding mean field streamline pattern shows a major circular vortex on the left side of the base, as shown in figure 21(b). This contributes to the asymmetric pressure distribution at the base, as observed in the top inset of figure 20(b) for  $C_q = 0$ . Moreover, this flow state resembles closely the  $P$  state of the natural (unactuated) flow at  $\beta = 0^\circ$ , albeit having a negligible secondary recirculation on the right side.

For  $C_q^{opt}$ , the blown jet volume is visibly confined within the main recirculation bubble, yet drifted towards the right under the prevailing yaw conditions. The recirculation bubble slightly recovers the lost symmetry with an increased recirculation length  $L_r^* = 1.46$ , contributing towards drag reduction. The increase in the length of recirculation bubble is 4 %, significantly lesser when compared with a 12 % increase observed for the  $\beta = 0^\circ$  experiments. Interestingly, the large circular vortex appears largely confined by the blown jet and shifted laterally towards the left side as well as downstream of the base. This contributes to a pressure recovery at the base and the transition of pressure gradient PDF towards the centre, as shown in the inset of figure 20(b) for  $C_q = 0.0063$ .

Flux exchange through the RRI is evaluated for the side-slip case, through a similar methodology presented in § 4.2. Figure 22 shows a comparison in the distribution of  $V_n^*$  for the  $C_q^0$  case at  $\beta = 5^\circ$  and the equivalent  $P$  state of the wake at  $\beta = 0^\circ$ . The flux analysis reveals that the  $\beta = 5^\circ$  case presents an increased influx  $\Phi_c = 0.1663$  compared with  $\Phi_c = 0.1529$  observed for the  $\beta = 0^\circ$  case. This may be attributed to the requirement of the fluid to replenish a larger cavity behind the bluff body, since at a side-slip angle the free-stream experiences a greater projected cross-section of the base. Similar to  $\beta = 0^\circ$ , base blowing for the  $\beta = 5^\circ$  case results in a decrease in influx  $\Phi_c = 0.1264$  accompanied by a concomitant reduction in  $\Phi_{a+b}$ . We can also observe from the  $V_n^*$  distribution for  $\beta = 5^\circ$  that the side towards the large recirculation is the primary contributor to supply the replenishment influx (see darker shade of  $V_n^{*(-)}$  on the RRI). With the same analogy,

## Equilibrium of fluxes in the wake of a 3-D bluff body

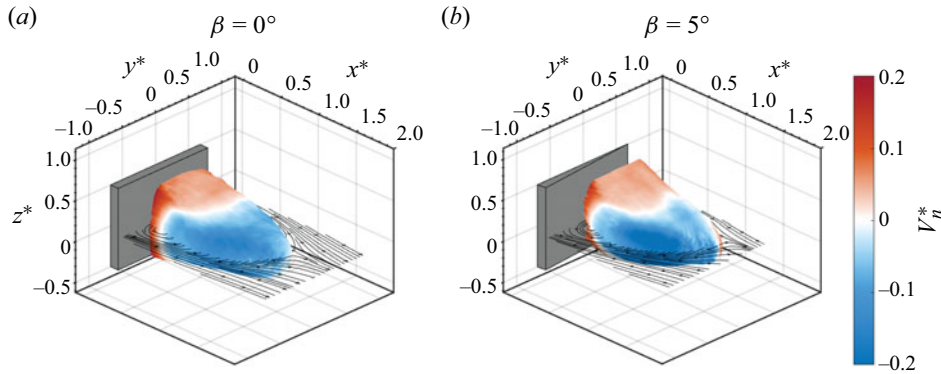


Figure 22. Normal velocity ( $V_n^*$ ) distribution on the RRI of the conditionally averaged  $P$ -state wake at  $\beta = 0^\circ$  and the ensemble-averaged wake at  $\beta = 5^\circ$ . Both representations are for the unactuated  $C_q^0$  case.

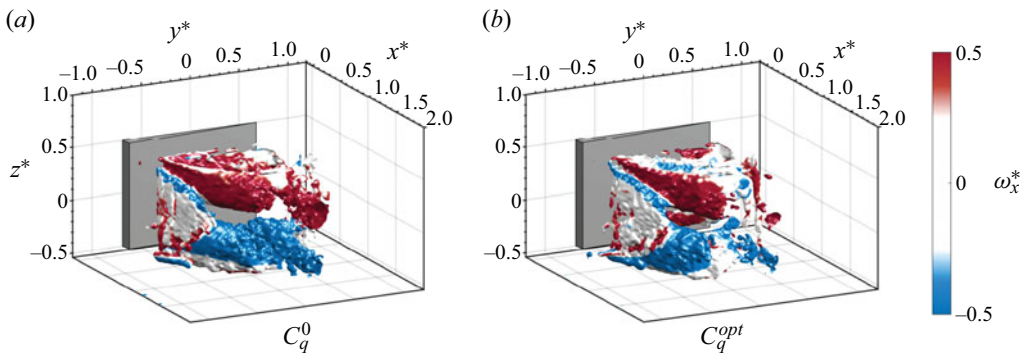


Figure 23. Wake structures for the unactuated flow and optimal blowing case at side slip  $\beta = 5^\circ$ . The structures are visualized through the isosurface of  $Q^* = 0.4$ , coloured by vorticity component ( $\omega_x^*$ ) in the longitudinal direction.

and consistent with the discussion in § 4.4, we can say that a major part of the influx requirement for the  $P$ -state wake shown in figure 22 is primarily met through the shear layer roll-up on the  $y^* < 0$  side of the base.

### 6.3. Flow structures under side slip

The wake structures for the two cases are obtained as isosurfaces of  $Q^* = 0.4$ , as shown in figure 23. For  $C_q^0$ , we observe a single dominant structure that appears as a hairpin vortex. This structure stems from the large recirculation at the left side of the base and ends as two tails on the opposite side of the vertical plane of symmetry. Again, the continuity in the distribution of the longitudinal component of vorticity ( $\omega_x^*$ ) confirms the origin of these tails back to the left side of the base. It is then interesting to note that this structure has resemblance to the main hairpin structure of the symmetry-breaking state for the natural flow at  $\beta = 0^\circ$ . The difference is in the two mirrored states; sampled  $N$  state for the  $\beta = 0^\circ$  case and  $P$  state for  $\beta = 5^\circ$  by analogy to the main recirculation location, and the absence of the secondary ‘C’-shaped horseshoe structure for the side-slip case. For  $C_q^{opt}$ , the main structure appears confined to the left side of the base, as observed by discontinuity of the vorticity distribution as well as disintegration of both tail structures. A secondary

horseshoe structure starts to appear on the right side of the base, but significantly weaker compared with the symmetrized pair of horseshoe structures observed for the optimal blowing case at  $\beta = 0^\circ$ .

## 7. Concluding remarks

The wake behind a flat-back Ahmed body is modified by steady blowing through a square orifice centrally located at the base of the body. In addition to the expected drag reduction, the base blowing also causes the wake to regain symmetry. The time-averaged, 3-D wake is captured and reconstructed using the SSPIV technique for several distinct blowing regimes. The mass fluxes in and out of the reconstructed mean wake are analysed using methods inspired by Stella *et al.* (2018) and related to the mechanisms responsible for establishing the recirculation length as originally described by Gerrard (1966) for a 2-D cylinder, and adapted to the 3-D bluff body wake by Lorite-Díez *et al.* (2020b). The measurement and evaluation of the mass flux caused by entrainment of the separated shear layers ( $\Phi_b$ ) and its contributions to the global equilibrium are performed for the first time for a 3-D turbulent wake.

The accounting of wake mass fluxes reveals a striking reduction of the influx of fluid replenishing the wake ( $\Phi_c$ ) whenever the recirculation region is enlarged by actuation. The influx of inviscid flow into the recirculation region of the wake is performed at the region's closure by the roll-up of the separated shear layers into the global mode vortex structures. The same vortices are responsible for taking out a major part of the recirculation region fluid mass when they are shed in the form of engulfment outflux ( $\Phi_a$ ). As suggested in the model of Lorite-Díez *et al.* (2020b), fluxes  $\Phi_a$  and  $\Phi_c$  are closely related via the global mode, but unlike in their mass regime these fluxes are modified by actuation and not preserved. It has been observed in several works before for both 2-D and 3-D bluff bodies that the global mode is damped when the recirculation bubble is elongated. Indeed, in the current measurements, the strength of the vortex roll-up evaluated through  $\sqrt{v'^{*2} + w'^{*2}}$  is well correlated with the magnitude of the influx  $\Phi_c$  (see figure 10(d) and table 2), and both are inversely proportional to  $L_r^*$ . At the same time, the total flux of fluid leaving the wake through the entrainment of the shear layers is very slightly modified in both  $C_q^{lo}$  and  $C_q^{opt}$  cases. Although the surface area over which this flux acts is increased with the larger recirculation length, the entrainment capacity of the shear layers is reduced. These results indicate that the delay of shear layer roll-up is achieved through a reduction of their growth rates similar to what was observed in Veerasamy *et al.* (2022). For the case of the mass regime, the shear layer entrainment flux is expected to increase (Lorite-Díez *et al.* 2020b); unfortunately, this could not be confirmed in the current experiment since the PIV was not performed for a  $C_q$  that would correspond to such a regime.

We can summarize that as the recirculation length is increased, the rate at which fluid is exchanged between the free-stream flow and the bluff body wake is decreased. The reduction of the replenishment influx is much greater than the flux of mass injection; the two do not compensate for each other mass wise. Thus, there is no need for the shear layers to increase their entrainment in order to evacuate the additional fluid mass, since the damping of the vortex roll-up at bubble closure reduces the amount of fluid attracted into the recirculation region in the first place. The momentum of fluid injection through the central blowing is identified as the dominant contribution in this process. A new favourable momentum regime term is coined, which describes a wake where the actuation momentum provokes a greater drag reduction, and the change of base suction is no longer in an affine relationship with the blowing coefficient.

The coherent structures corresponding to the symmetry-breaking mode are identified, through POD, as an interacting pair of a major hairpin structure and a secondary horseshoe vortex. The hairpin structure originates from the large recirculation of the asymmetric flow and presents similarities to the structure observed under side-slip conditions. The hairpin structure was recently observed by Pavia *et al.* (2020) using tomographic PIV. We show that the POD applied on the present time-unresolved SPIV fields is able to recover the mode corresponding to the bistable dynamics of the wake. The optimal blowing case presents a pair of weakened horseshoe structures parallel to the base resembling a toroidal structure.

The effectiveness of central base blowing is examined for the model at side slip  $\beta = 5^\circ$ . Compared with the  $\beta = 0^\circ$  case, the unactuated wake presents a smaller recirculation length corresponding to an increased drag configuration. Drag reduction is achieved through an elongation of the recirculation region along with a reduction of the wake asymmetry strength. Flux analysis reveals a greater influx  $\Phi_c$  requirement of the wake to replenish a larger cavity behind the body at  $\beta = 5^\circ$ . The elongation of the recirculation bubble is again accompanied by a concomitant reduction of  $\Phi_c$ .





The work presented here offers a methodology of accounting for mass fluxes in turbulent wakes to assess the core mechanisms of the recirculation region equilibrium. The analysis of mass fluxes for the bistable, unactuated wake reveals that the ensemble-averaged flow does not provide a realistic value for the replenishment influx, and that conditionally averaged flow for either  $P$  or  $N$  state must be used for that purpose. Moreover, the flux distribution indicates that the primary contribution of the replenishment fluid comes from the low-pressure recirculation side of the asymmetric state of the wake (see figures 7(b) and 22). The two observations above lead to a possibility that the wake has a specific requirement for replenishment fluid based on the bluff body geometry and flow conditions, and that the asymmetric flow features of the wake may be the key to fulfilling this requirement. We propose that the methodology outlined in this paper should be applied to flow cases such as the perimetric slit blowing where the bubble is enlarged but remains asymmetric, and the base cavity configuration where there is no mass addition but symmetry is regained. Analysing the wake fluxes in each case might lead to a more fundamental understanding of the root causes of asymmetric wakes of 3-D bluff bodies in general.

**Acknowledgements.** The authors are grateful to A. Kourta, N. Mazellier and M. Lorite-Díez for fruitful discussions. We would also like to thank T. Pichon and L. Cherfa of the ENSTA-UME, and R. De Jesus and R. Ganithi of the KU Fabrication Laboratory, for their exceptional support in this experiment.

**Funding.** This work has been supported by the Khalifa University of Science and Technology under award nos. CIRA-2019-025 and RIG-2023-024.

**Declaration of interests.** The authors report no conflict of interest.

#### Author ORCIDs.

-  T.I. Khan <https://orcid.org/0000-0001-7746-6608>;
-  L. Pastur <https://orcid.org/0000-0003-0038-5898>;
-  O. Cadot <https://orcid.org/0000-0001-7323-6418>;
-  V. Parezanović <https://orcid.org/0000-0002-4396-2686>.

#### REFERENCES

- AHMED, D. & MORGANS, A.S. 2022 Nonlinear feedback control of bimodality in the wake of a three-dimensional bluff body. *Phys. Rev. Fluids* **7** (8), 084401.

- AHMED, S.R., RAMM, G. & FALTIN, G. 1984 Some salient features of the time-averaged ground vehicle wake. *SAE Technical Paper* 840300. <https://doi.org/10.4271/840300>.
- BAO, D., BORÉE, J., HAFFNER, Y. & SICOT, C. 2022 Near wake interactions and drag increase regimes for a square-back bluff body. *J. Fluid Mech.* **936**, A2.
- BARROS, D., BORÉE, J., CADOT, O., SPOHN, A. & NOACK, B.R. 2017 Forcing symmetry exchanges and flow reversals in turbulent wakes. *J. Fluid Mech.* **829**, R1.
- BARROS, D., BORÉE, J., NOACK, B.R., SPOHN, A. & RUIZ, T. 2016 Bluff body drag manipulation using pulsed jets and coanda effect. *J. Fluid Mech.* **805**, 422–459.
- BEARMAN, P.W. 1967 The effect of base bleed on the flow behind a two-dimensional model with a blunt trailing edge. *Aeronaut. Q.* **18** (3), 207–224.
- BONNAVION, G. & CADOT, O. 2018 Unstable wake dynamics of rectangular flat-backed bluff bodies with inclination and ground proximity. *J. Fluid Mech.* **854**, 196–232.
- BONNAVION, G. & CADOT, O. 2019 Boat-tail effects on the global wake dynamics of a flat-backed body with rectangular section. *J. Fluids Struct.* **89**, 61–71.
- BRACKSTON, R.D., DE LA CRUZ, J.M.G., WYNN, A., RIGAS, G. & MORRISON, J.F. 2016 Stochastic modelling and feedback control of bistability in a turbulent bluff body wake. *J. Fluid Mech.* **802**, 726–749.
- BURTON, D., WANG, S., SMITH, D.T., SCOTT, H.N., CROUCH, T.N. & THOMPSON, M.C. 2021 The influence of background turbulence on Ahmed-body wake bistability. *J. Fluid Mech.* **926**, R1.
- CADOT, O., ALMARZOOQI, M., LEGEAI, A., PAREZANOVIĆ, V. & PASTUR, L. 2020 On three-dimensional bluff body wake symmetry breaking with free-stream turbulence and residual asymmetry. *C. R. Méc.* **348** (6–7), 509–517.
- CADOT, O., EVRARD, A. & PASTUR, L. 2015 Imperfect supercritical bifurcation in a three-dimensional turbulent wake. *Phys. Rev. E* **91** (6), 063005.
- CHOI, H., LEE, J. & PARK, H. 2014 Aerodynamics of heavy vehicles. *Annu. Rev. Fluid Mech.* **46**, 441–468.
- DE LA CRUZ, J.M.G., OXLADE, A.R. & MORRISON, J.F. 2017 Passive control of base pressure on an axisymmetric blunt body using a perimetric slit. *Phys. Rev. Fluids* **2** (4), 043905.
- DALLA-LONGA, L., EVSTAFYEVA, O. & MORGANS, A.S. 2019 Simulations of the bi-modal wake past three-dimensional blunt bluff bodies. *J. Fluid Mech.* **866**, 791–809.
- DANDOIS, J., GARNIER, E. & SAGAUT, P. 2007 Numerical simulation of active separation control by a synthetic jet. *J. Fluid Mech.* **574**, 25–58.
- DUELL, E.G. & GEORGE, A.R. 1993 Measurements in the unsteady near wakes of ground vehicle bodies. *Tech. Rep.* SAE Technical Paper.
- EVRARD, A., CADOT, O., HERBERT, V., RICOT, D., VIGNERON, R. & DÉLERY, J. 2016 Fluid force and symmetry breaking modes of a 3D bluff body with a base cavity. *J. Fluids Struct.* **61**, 99–114.
- EVSTAFYEVA, O., MORGANS, A.S. & DALLA-LONGA, L. 2017 Simulation and feedback control of the Ahmed body flow exhibiting symmetry breaking behaviour. *J. Fluid Mech.* **817**, R2.
- FAN, Y., PAREZANOVIĆ, V. & CADOT, O. 2022 Wake transitions and steady-instability of an Ahmed body in varying flow conditions. *J. Fluid Mech.* **942**, A22.
- GERRARD, J.H. 1966 The mechanics of the formation region of vortices behind bluff bodies. *J. Fluid Mech.* **25** (2), 401–413.
- GILLIÉRON, P. & KOURTA, A. 2010 Aerodynamic drag reduction by vertical splitter plates. *Exp. Fluids* **48** (1), 1–16.
- GRANDEMANGE, M., CADOT, O., COURBOIS, A., HERBERT, V., RICOT, D., RUIZ, T. & VIGNERON, R. 2015 A study of wake effects on the drag of Ahmed's squareback model at the industrial scale. *J. Wind Engng Ind. Aerodyn.* **145**, 282–291.
- GRANDEMANGE, M., CADOT, O. & GOHLKE, M. 2012 Reflectional symmetry breaking of the separated flow over three-dimensional bluff bodies. *Phys. Rev. E* **86** (3), 035302.
- GRANDEMANGE, M., GOHLKE, M. & CADOT, O. 2013a Bi-stability in the turbulent wake past parallelepiped bodies with various aspect ratios and wall effects. *Phys. Fluids* **25** (9), 095103.
- GRANDEMANGE, M., GOHLKE, M. & CADOT, O. 2013b Turbulent wake past a three-dimensional blunt body. Part 1. Global modes and bi-stability. *J. Fluid Mech.* **722**, 51–84.
- GRANDEMANGE, M., GOHLKE, M. & CADOT, O. 2014 Turbulent wake past a three-dimensional blunt body. Part 2. Experimental sensitivity analysis. *J. Fluid Mech.* **752**, 439–461.
- GRANDEMANGE, M., MARY, A., GOHLKE, M. & CADOT, O. 2013c Effect on drag of the flow orientation at the base separation of a simplified blunt road vehicle. *Exp. Fluids* **54** (5), 1529.
- HAFFNER, Y., BORÉE, J., SPOHN, A. & CASTELAIN, T. 2020 Mechanics of bluff body drag reduction during transient near-wake reversals. *J. Fluid Mech.* **894**, A14.
- HAFFNER, Y., CASTELAIN, T., BORÉE, J. & SPOHN, A. 2021 Manipulation of three-dimensional asymmetries of a turbulent wake for drag reduction. *J. Fluid Mech.* **912**, A6.



## Equilibrium of fluxes in the wake of a 3-D bluff body

- HESSE, F. & MORGANS, A.S. 2021 Simulation of wake bimodality behind squareback bluff-bodies using LES. *Comput. Fluids* **223**, 104901.
- HOLMES, P., LUMLEY, J.L. & BERKOOZ, G. 2010 *Turbulence, Coherent Structures, Symmetry and Dynamical Systems*. Cambridge University Press.
- HSU, E.C., PASTUR, L., CADOT, O. & PAREZANOVIĆ, V. 2021 A fundamental link between steady asymmetry and separation length in the wake of a 3D square-back body. *Exp. Fluids* **62**, 95.
- HUCHO, W. & SOVRAN, G. 1993 Aerodynamics of road vehicles. *Annu. Rev. Fluid Mech.* **25** (1), 485–537.
- HUNT, J.C.R., WRAY, A.A. & MOIN, P. 1988 Eddies, streams, and convergence zones in turbulent flows. In *Studying Turbulence Using Numerical Simulation Databases, 2. Proceedings of the 1988 Summer Program*.
- KEIRSBULCK, L., CADOT, O., BASLEY, J. & LIPPERT, M. 2023 Base suction, entrainment flux, and wake modes in the vortex formation region at the rear of a three-dimensional blunt bluff body. *Phys. Rev. E* **108** (1), 015101.
- KHALIGHI, B., CHEN, K.H. & IACCARINO, G. 2012 Unsteady aerodynamic flow investigation around a simplified square-back road vehicle with drag reduction devices. *J. Fluids Engng* **134** (6), 061101.
- KHAN, T.I., PAREZANOVIĆ, V. & AFGAN, I. 2023 Capturing the bi-stable asymmetry exchanges in the turbulent air wake of a simplified frigate using large eddy simulation. *Intl J. Heat Fluid Flow* **104**, 109233.
- KHAN, T.I., PAREZANOVIĆ, V., PASTUR, L. & CADOT, O. 2022a Suppression of the wake steady asymmetry of an Ahmed body by central base bleed. *Phys. Rev. Fluids* **7** (8), 083902.
- KHAN, T.I., TAJIK, A.R. & PAREZANOVIĆ, V. 2022b Drag reduction of a generic transport vehicle model using a fluidic oscillator. *Intl J. Thermofluids* **15**, 100180.
- LI, R., BARROS, D., BORÉE, J., CADOT, O., NOACK, B.R. & CORDIER, L. 2016 Feedback control of bimodal wake dynamics. *Exp. Fluids* **57**, 158.
- LITTLEWOOD, R.P. & PASSMORE, M.A. 2012 Aerodynamic drag reduction of a simplified squareback vehicle using steady blowing. *Exp. Fluids* **53** (2), 519–529.
- LORITE-DÍEZ, M., JIMÉNEZ-GONZÁLEZ, J.I., PASTUR, L., CADOT, O. & MARTÍNEZ-BAZÁN, C. 2020a Drag reduction of three-dimensional bodies by base blowing with various gas densities. *Phys. Rev. E* **102** (1), 011101(R).
- LORITE-DÍEZ, M., JIMÉNEZ-GONZÁLEZ, J.I., PASTUR, L., MARTÍNEZ-BAZÁN, C. & CADOT, O. 2020b Experimental analysis of the effect of local base blowing on three-dimensional wake modes. *J. Fluid Mech.* **883**, A53.
- LUCAS, J.M., CADOT, O., HERBERT, V., PARPAIS, S. & DÉLERY, J. 2017 A numerical investigation of the asymmetric wake mode of a squareback Ahmed body – effect of a base cavity. *J. Fluid Mech.* **831**, 675–697.
- OXLADE, A.R., MORRISON, J.F., QUBAIN, A. & RIGAS, G. 2015 High-frequency forcing of a turbulent axisymmetric wake. *J. Fluid Mech.* **770**, 305–318.
- PAREZANOVIĆ, V. & CADOT, O. 2012 Experimental sensitivity analysis of the global properties of a two-dimensional turbulent wake. *J. Fluid Mech.* **693**, 115–149.
- PAVIA, G., PASSMORE, M. & SARDU, C. 2018 Evolution of the bi-stable wake of a square-back automotive shape. *Exp. Fluids* **59**, 20.
- PAVIA, G., PASSMORE, M.A., VARNEY, M. & HODGSON, G. 2020 Salient three-dimensional features of the turbulent wake of a simplified square-back vehicle. *J. Fluid Mech.* **888**, A33.
- PERRY, A.K., PAVIA, G. & PASSMORE, M. 2016 Influence of short rear end tapers on the wake of a simplified square-back vehicle: wake topology and rear drag. *Exp. Fluids* **57**, 169.
- PIER, B. 2008 Local and global instabilities in the wake of a sphere. *J. Fluid Mech.* **603**, 39–61.
- PLUMEJEAU, B., KEIRSBULCK, L., DELPRAT, S., LIPPERT, M. & ABASSI, W. 2020 Behavior of the square-back Ahmed body global modes at low ground clearance. *Phys. Rev. Fluids* **5** (8), 084701.
- PORTEIRO, J.L.F., PRZIREMBEL, C.E.G. & PAGE, R.H. 1983 Modification of subsonic wakes using boundary layer and base mass transfer. *AIAA J.* **21** (5), 665–670.
- SEVILLA, A. & MARTÍNEZ-BAZÁN, C. 2004 Vortex shedding in high Reynolds number axisymmetric bluff-body wakes: local linear instability and global bleed control. *Phys. Fluids* **16** (9), 3460–3469.
- STELLA, F., MAZELLIER, N., JOSEPH, P. & KOURTA, A. 2018 Mass entrainment-based model for separating flows. *Phys. Rev. Fluids* **3** (11), 114702.
- STELLA, F., MAZELLIER, N. & KOURTA, A. 2017 Scaling of separated shear layers: an investigation of mass entrainment. *J. Fluid Mech.* **826**, 851–887.
- SURYANARAYANA, G.K. & MEIER, G.E.A. 1995 Effect of ventilation on the flowfield around a sphere. *Exp. Fluids* **19** (2), 78–88.
- TANNER, M. 1975 Reduction of base drag. *Prog. Aerosp. Sci.* **16** (4), 369–384.
- THACKER, A., AUBRUN, S., LEROY, A. & DEVINANT, P. 2010 Unsteady analyses of the flow separation on the rear window of a simplified ground vehicle model. In *28th AIAA Applied Aerodynamics Conference*. American Institute of Aeronautics and Astronautics.

- VEERASAMY, D., TAJIK, A.R., PASTUR, L. & PAREZANOVIĆ, V. 2022 Effect of base blowing by a large-scale fluidic oscillator on the bistable wake behind a flat-back Ahmed body. *Phys. Fluids* **34** (3), 035115.
- VISWANATH, P.R. 1996 Flow management techniques for base and afterbody drag reduction. *Prog. Aerosp. Sci.* **32** (2–3), 79–129.
- VOLPE, R., DEVINANT, P. & KOURTA, A. 2015 Experimental characterization of the unsteady natural wake of the full-scale square back Ahmed body: flow bi-stability and spectral analysis. *Exp. Fluids* **56**, 99.
- WASSEN, E., EICHINGER, S. & THIELE, F. 2010 Simulation of active drag reduction for a square-back vehicle. In *Active Flow Control II* (ed. R. King), pp. 241–255. Notes on Numerical Fluid Mechanics and Multidisciplinary Design. Springer.
- WEISS, J. 2019 A tutorial on the proper orthogonal decomposition. In *AIAA Aviation 2019 Forum*. American Institute of Aeronautics and Astronautics.
- WONG, D.T.M. & MAIR, W.A. 1983 Boat-tailed afterbodies of square section as drag-reduction devices. *J. Wind Engng Ind. Aerodyn.* **12** (2), 229–235.
- WOOD, C.J. 1964 The effect of base bleed on a periodic wake. *Aeronaut. J.* **68** (643), 477–482.